System Identification of the Longitudinal/Heave Dynamics for a Tandem-Rotor Helicopter Including Higher-Order Dynamics

Michael A. Lawler[*]
US Army AMRDEC, Aviation Engineering Directorate, Redstone Arsenal, AL 35898

Christina M. Ivler[†]
San Jose State University Foundation, Moffett Field, CA 94035

Mark B. Tischler[‡]
US Army AMRDEC, Aeroflightdynamics Directorate, Moffett Field, CA 94035

and

Yuri B. Shtessel[§]
The University of Alabama in Huntsville, Huntsville, AL 35899

As part of a product improvement program to upgrade the CH-47F cockpit and flight control system for the US Army, a new Digital Automatic Flight Control System (DAFCS) is being developed by Boeing Helicopters. The DAFCS will incorporate modern control algorithms in the low-speed/hover regime to improve handling qualities for operations in a Degraded Visual Environment (DVE). In support of the modern control law development, the US Army required a complete closed-loop analysis model in SIMULINK®. The central element of this analysis model was an accurate state-space representation of the bare-airframe response. CIFER® was used to perform the system identification at three gross weights and two airspeeds having a common quasi-steady model structure. The quasi-steady model identification had a restricted frequency range due to rotor-on-rotor and inflow dynamics. Subsequently, the quasi-steady model was extended to higher-frequencies by incorporating higher-order rotor dynamics. This paper covers the identification of the longitudinal/heave-axis bare-airframe dynamics for the Heavy Gross Weight (HGW) hover configuration, and provides a comparison of results for the quasi-steady and hybrid models.

Nomenclature

a	=	airfoil lift curve slope, (rad^{-1}); or acceleration when subscripted with x, y, z
A	=	derivative for specific inflow "apparent mass" force
B	=	derivative for specific flapping (coning) moment
c	=	mean blade chord, (ft)
C_T	=	thrust coefficient
$\tilde{C}_T$	=	perturbation of thrust coefficient
C_0	=	dynamic inflow model factor (C_0 =1 for Pitt-Peters model, C_0 =0.639 for Carpenter-Fridovich model)
d_2, d_1, d_0	=	rotor-on-rotor torque mode 2nd order system denominator coefficients
F	=	designates forward rotor when subscript

[*] Aerospace Engineer, Aeromechanics Division, AMSRD-AMR-AE-A, Member AIAA
[†] Research Engineer, San Jose State University Foundation, Member AIAA
[‡] Senior Scientist, Flight Control Technology Group Leader, Associate Fellow AIAA
[§] Professor, Department of Electrical and Computer Engineering, 301 Sparkman Drive, Associate Fellow AIAA

$\boldsymbol{F}$	=	stability derivative matrix
g	=	acceleration due to gravity, (32.174 ft/sec^2)
$\boldsymbol{G}$	=	control derivative matrix
h	=	vertical distance from aircraft center-of-gravity to center of rotor hub, (ft)
$H, \boldsymbol{H}$	=	hub in-plane force; or output matrix when bold
I_{yy}	=	aircraft moment of inertia about y-axis, (slug-ft^2)
$\boldsymbol{J}$	=	output control matrix
K_{DCP}	=	control gain converting differential collective pitch inputs to effective blade root pitch angle, (rad/in)
K_θ	=	control gain converting collective pitch inputs to effective blade root pitch angle, (rad/in)
ℓ	=	longitudinal distance from aircraft center-of-gravity to center of rotor hub, (ft)
m	=	mass of aircraft, (slug)
$M, \boldsymbol{M}$	=	derivative for specific pitching moment; or hub moment; or modal matrix when bold
$\hat{M}$	=	derivative for specific higher-order pitching moment
Mf	=	derivative for pitch axis flapping moment
n_2, n_1, n_0	=	rotor-on-rotor torque mode 2nd order system numerator coefficients
p	=	fuselage roll rate, (rad/sec); + right wing down
q	=	fuselage pitch rate, (rad/sec); + nose up
r	=	fuselage yaw rate, (rad/sec); + nose right
R	=	rotor radius, (ft); or designates rear rotor when subscript
$\overline{R}(s)$	=	transfer function for rotor-on-rotor torque mode
s	=	Laplace transform variable
T	=	thrust, (lbf)
$\boldsymbol{u}$	=	control vector
u	=	longitudinal velocity in body-axis, (ft/sec); + forward
v	=	lateral velocity in body-axis, (ft/sec); + right
w	=	vertical velocity in body-axis, (ft/sec); + down
W	=	weight of aircraft, (lbf)
$\boldsymbol{x}$	=	state vector
X	=	derivative for specific longitudinal force
$\hat{X}$	=	derivative for specific higher-order longitudinal force
Y	=	derivative for specific lateral force
Z	=	derivative for specific vertical force
$\hat{Z}$	=	derivative for specific higher-order vertical force
β_0	=	coning angle, (rad); + up
β_{1c}	=	longitudinal flapping angle, (rad); + forward
β_{1s}	=	lateral flapping angle, (rad); + left
γ	=	Lock number
Δ	=	perturbation
$\delta_{col}, \delta_{COL}$	=	thrust lever control deflection input as measured at the pilot stick (*col*) or mixing unit (*COL*), (inches)
$\delta_{lon}, \delta_{LON}$	=	control deflection input as measured at the pilot stick (*lon*) or mixing unit (*LON*), (inches)
ζ	=	damping ratio
θ	=	fuselage pitch attitude, (rad)
$\overline{v}_0$	=	inflow ratio, $\left(\overline{v}_0 = +\sqrt{C_{T_0}/2}\,\right)$
ρ	=	air density, (slug/ft^3)
σ	=	rotor solidity ratio
τ_f	=	rotor flap time constant, (sec)
$\tau_{COL(LON)}$	=	equivalent time delay for collective (or longitudinal) axis, (sec)
υ	=	rotor dynamic inflow state
Ω	=	rotor speed, (rad/sec)
ω_n	=	natural frequency, (rad/sec)

I. Introduction

AT the request of the US Army, Boeing Helicopters is currently developing a Digital Automatic Flight Control System (DAFCS) upgrade for the CH-47F Chinook helicopter to replace the obsolete analog flight controllers. The CH-47 analog AFCS was originally designed to meet the requirements of MIL-H-8501, *General Requirements for Helicopter Flying and Ground Handling Qualities* (dated 5 Nov 1952). This military specification was updated to Rev. A (MIL-H-8501A) in September of 1961; which remained in effect until it was canceled without replacement in August of 1995. In addition, the analog AFCS control laws were designed for operations in day Visual Meteorological Conditions (VMC) at altitude.

In contrast to original mission requirements, the Army is currently placing greater emphasis on operations at night and in a Degraded Visual Environment (DVE). As a result of this mission creep, pilot workload has increased and handling qualities have deteriorated— especially in low-speed/hover near-earth operations. The original performance specification requirements are antiquated and outdated in light of today's operational demands and the need to safely operate in a DVE. Much research has been accomplished over the last two decades to develop improved performance specifications[1,2] to address handling qualities requirements and the control response-types[3,4,5] needed for safe DVE operations.

The new digital Flight Control Computers (FCCs) for the CH-47F are being integrated into the existing legacy flight control system and therefore maintain the limited-, partial-authority architecture. However, recent research[6,7] has shown that the modern control algorithms developed to address handling qualities shortcomings in a DVE are capable of being successfully implemented in a limited-authority AFCS. Based upon this research and flight-test demonstrations, the US Army directed Boeing to incorporate an attitude command response-type as the baseline architecture at low-speed/hover and a selectable translational rate command response-type with position hold for precision maneuvering within a DVE.[8]

Frequency-Domain system identification methods were used extensively in this program, to include:
1) Development of state-space models of bare-airframe dynamics for flight control analysis and optimization
2) Analysis of closed-loop handling-qualities
3) Modeling and validation of DAFCS components
4) Determination of flight control stability margins and
5) Validation and improvement of physics-based models

This paper will focus solely on the first application. In support of the flight control development, the US Army required a complete closed-loop analysis model in SIMULINK®. The central element of this analysis model was an accurate state-space representation of the bare-airframe response— especially in the Heavy Gross Weight (HGW) configuration where reduced stability margins were anticipated. System identification studies were conducted based upon the frequency-sweep flight-test data, and state-space dynamics models of the CH-47F bare-airframe responses were determined for three weight conditions in hover and forward flight.

This paper presents the HGW hover modeling effort for the longitudinal/heave-axis bare-airframe dynamics associated with the DAFCS flight-test program using CIFER® (performed by the 2nd and 3rd authors); as well as a graduate research project (performed by the 1st author) to extend the identified state-space model to higher frequencies by implementing higher-order dynamic modes into the model architecture using the hybrid-model structure developed by Tomashofski and Tischler.[9] The two models are compared in terms of frequency-domain match to flight data, time-domain match to flight data, and accuracy of control system stability metrics.

A. Objective for Frequency-Domain Flight Testing

The objective of the frequency-domain flight testing was to gather sufficient data for the system identification at various operating points within the flight envelope, at various aircraft gross weights, so as to ensure the control algorithms were robust over a representative flight envelope. Test conditions for the frequency-domain testing are given in Table 1. As stated earlier, this paper will focus only on the system identification for the HGW configuration, at the hover condition, as it was deemed the most critical.

Table 1. Frequency-sweep test conditions.

Aircraft Configuration	Approximate Gross Weight (lb)	Longitudinal Center of Gravity (in)	Pressure Altitude (ft)	Airspeed (KIAS)
Light	33,000	nominal	Field	0
			5000	60
Medium	41,000	nominal	Field	0
			5000	60
Heavy	48,000	nominal	Field	0
			5000	60

B. Description

1. General Aircraft Description

The CH-47F is a twin turbine-engine, tandem-rotor helicopter designed for transportation of cargo and troops during day or night in visual or instrument meteorological conditions. The helicopter is equipped with two Honeywell T55-GA-714A engines. The two engines simultaneously drive the tandem, three-bladed, fully-articulated, counter-rotating rotors through engine transmissions, a combining transmission, drive shafting, and reduction gearboxes. The forward transmission is located at the forward pylon above the cockpit. The combining transmission, drive shafting, and aft transmission are located in the aft pylon area. Drive shafting from the combining transmission runs along the top of the fuselage to the forward transmission. The helicopter is equipped with four fixed landing gear and a hydraulically powered loading ramp at the rear of the cargo compartment. The pilot (right seat) and co-pilot (left seat) are seated in a side-by-side configuration with dual flight controls. The DAFCS test aircraft is depicted in Figure 1.

Figure 1. CH-47F Chinook DAFCS test aircraft.

2. Aircraft Modifications

The test aircraft has been modified to include two primary product improvements: 1) the Digital Automatic Flight Control System (DAFCS) and 2) the Common Avionics Architecture System (CAAS). The DAFCS provides a digital Flight Control Computer (FCC) replacement for the current, obsolete analog AFCS controller; and in addition incorporates modern control algorithms to improve low-speed/hover handling qualities and maneuverability. The new Digital FCCs are integrated into the legacy mechanical flight control system, and therefore maintain the existing limited-, partial-authority architecture. The CAAS is an avionics suite upgrade that replaces analog gauges with a glass cockpit providing full integration of communication, navigation and air vehicle systems through a Rockwell-Collins designed pilot interface utilizing five multi-function displays and two control display units.

3. Flight Control System

The helicopter is controlled by changing the pitch of the blades on both rotor heads either collectively or cyclically. The flight control system consists of lower and upper hydraulic actuation systems, two dual digital FCCs, and a mechanical linkage system that mixes and transmits control motions from the cockpit controls to the rotor heads.

The lower hydraulic system consists of the Integrated Lower Control Actuators (ILCAs) which aide the pilot in moving the upper flight controls via a boost actuator. The ILCA also includes dual-redundant Extensible Link Actuators (ELAs), controlled by the FCCs, providing stability and control augmentation in the pitch, roll, and yaw axes. The thrust ILCA does not have ELAs and therefore provides only boost-assist to the pilot. The upper hydraulic actuation system includes the pivoting and swiveling Upper Boost Actuators (UBAs) at each swashplate, which are actuated via the upper mechanical controls following mechanical control mixing.

Pitch, roll and yaw changes are controlled through movement of the pilot's (or copilot's) flight controls which include a thrust control lever (in the Chinook the collective control is properly called thrust control), a cyclic control stick, and directional pedals. The pilot's controls are interconnected beneath the cockpit floor with the copilot's controls. Flight control movements are transmitted through a system of bellcranks, push-pull tubes, and actuators to a mixing unit just aft of the cockpit.

The control movements are mixed to give the correct lateral cyclic and collective pitch motions to the rotors through the dual UBAs under each swashplate. The helicopter is controlled vertically with the thrust control lever. Thrust control inputs yield an equal and simultaneous increase or decrease in the pitch of all blades on both rotors, thereby causing the helicopter to ascend or descend vertically. Thrust control movements are illustrated in Figure 2.
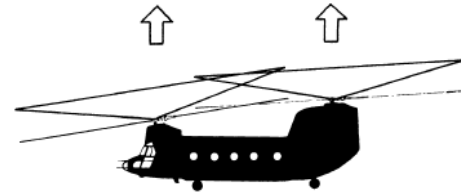
Directional control is achieved with the directional pedals by imparting equal but opposite (i.e., differential) lateral cyclic pitch to the forward and rear rotor blades respectively; thus causing the Tip Path Plane (TPP) of each rotor to tilt in opposite directions. For example, moving the right pedal forward causes the forward rotor TPP to tilt to the right, whereas the rear rotor TPP will tilt to the left, resulting in a clockwise directional moment about the center of gravity as illustrated in Figure 3. Conversely, a left pedal input causes a counter-clockwise directional moment.
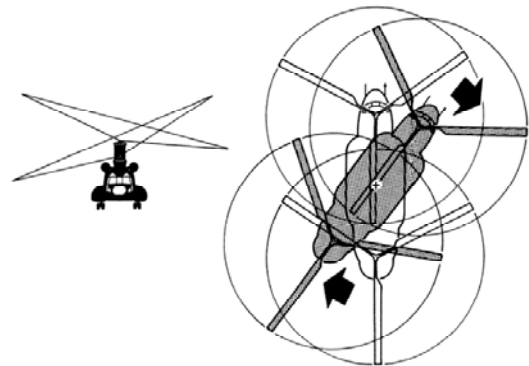
Lateral control is achieved by applying equal lateral cyclic pitch to the blades with the cyclic control stick. Moving the cyclic control stick to the left results in both rotors' TPP tilting to the left as illustrated in Figure 4. Conversely, a right cyclic input tilts both rotors' TPP to the right.
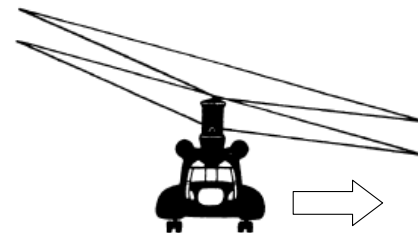
The tandem rotor helicopter is controlled longitudinally with the cyclic control stick using Differential Collective Pitch (DCP); whereby the pitch of the forward and rear rotor blades are all collectively changed equally yet in the opposite direction. Moving the cyclic control stick forward simultaneously causes a decrease in collective pitch on the forward rotor and an increase in collective pitch on the rear rotor, thereby creating a nose-down pitching moment about the helicopter's center of gravity as illustrated in Figure 5. Conversely, an aft cyclic input creates a nose-up pitching moment.
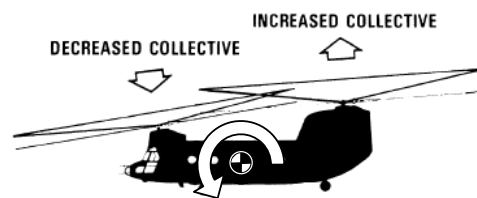
In addition to the control movements described above, combinations of directional pedal and lateral cyclic inputs generate unique motions of the helicopter, permitting the helicopter to directionally rotate about either the forward or rear rotor. This control flexibility makes the Chinook very maneuverable in tight quarters.

II. Methodology

The system identification approach used in this project is the Frequency-Response Method, as illustrated in the flowchart in Figure 6 and implemented in the CIFER® package. Each of the elements of the flowchart will be briefly described in this section. A complete discussion of the flight testing and analysis methods is given by Tischler and Remple.[10]

The Frequency-Response Method is well suited to the accurate characterization of fixed-wing and rotary-wing aircraft dynamics from flight data. The resulting models are useful in a wide range of applications, including control system design, handling-qualities analysis, and the determination and validation of simulation math models.
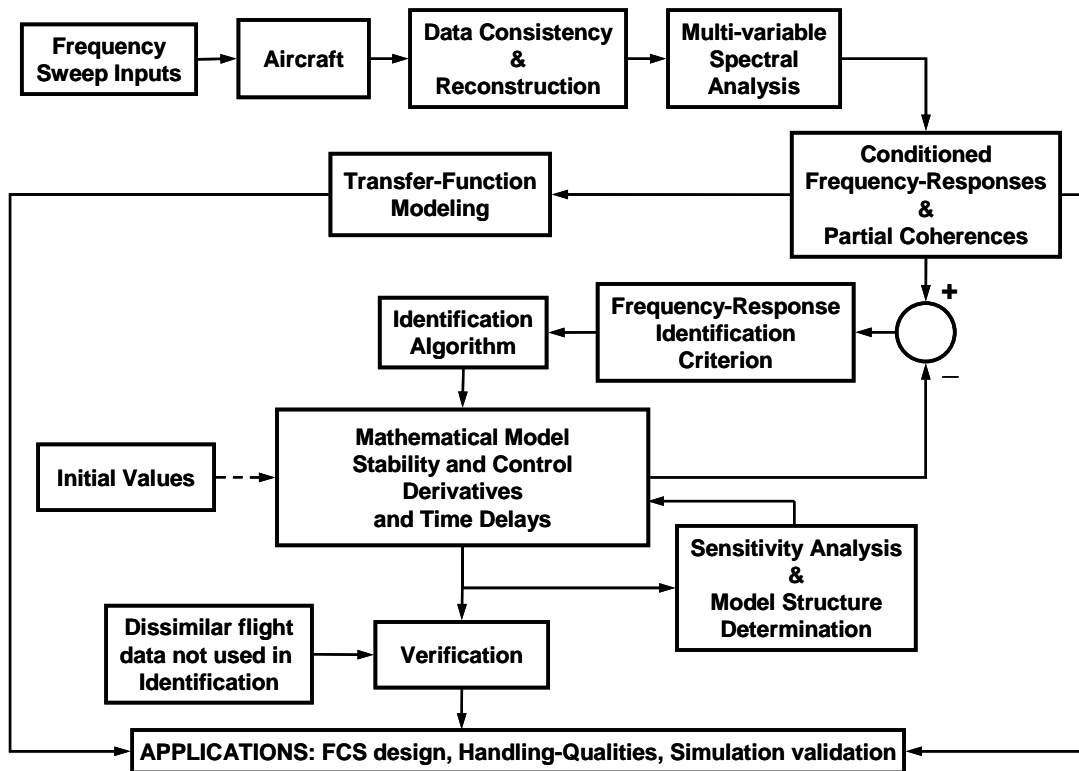

Figure 2. Rotor system response to thrust control.

Figure 3. Rotor system response to directional pedals.

Figure 4. Rotor system response to lateral cyclic control.

Figure 5. Rotor system response to longitudinal cyclic control.

Figure 6. System identification approach using frequency-response method.

The method uses dynamic response time-history test data (e.g., from flight, piloted simulation, bench tests) generated from pilot or computer generated inputs, such as sweeps or other inputs with good spectral content. These inputs excite the system vehicle dynamics, which could be an aircraft or any other physical system or subsystem (e.g., actuators, filters) of interest. In the CH-47 project, both piloted and automated sweeps inputs were used. Details on frequency-sweep flight-testing methodology are given in Ham et al.[11] A piloted longitudinal sweep time history for the CH-47F is shown in Figure 7. The frequency sweep begins at low frequency and increases smoothly in frequency until the maximum frequency is reached. This slow buildup in frequency ensures excitation of all dynamics within the frequency range of interest.
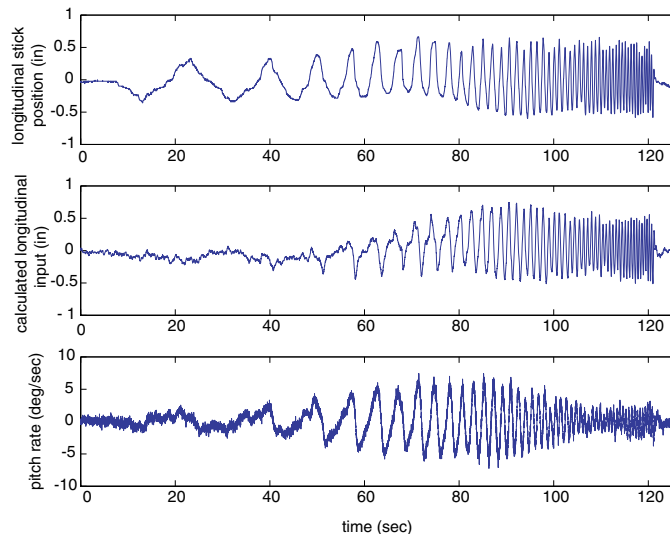
After conducting the aircraft tests and collecting measurement data, the next step is to check that the database is internally consistent and, to the extent possible, free of spurious noise before actually starting the identification process. The SMACK[12] tool is used in this project for data consistency analysis, data reconstruction, and transfer of measurements to the aircraft center-of-gravity.

Figure 7. CH-47F example frequency sweep flight test.

The next step is to perform a multi-variable spectral analysis of the data. This analysis, which is a multi-input/multi-output (MIMO) matrix generalization of the simple single-input/single-output (SISO) FFT, is necessary

American Institute of Aeronautics and Astronautics

for most aircraft system identification applications since real flight-test data inevitably involves multiple, partially correlated, control inputs during a single excitation maneuver. The MIMO frequency-response matrix constitutes a nonparametric model of the aircraft response, since it fully characterizes the input-to-output behavior without the need for defining a model structure or determining model parameters. An important by-product of this analysis is the coherence function, which provides key information about the frequency-response accuracy. When the dynamics contain nonlinear behavior, the frequency-response function as extracted using the Fourier transform is the describing function, which is the linear model that best characterizes the nonlinear behavior of the system.[13] As shown in the flowchart, the nonparametric modeling results support many direct applications, including the design and analysis of flight control systems, stability margin determination, piloted handling-qualities analysis, and the validation and improvement of simulation models. These analyses were an important aspect of the CH-47F DAFCS development, but are not discussed in this paper.

Two key features of the Frequency-Response Method as implemented in CIFER® are the chirp z-transform and composite window optimization. The chirp z-transform is an advanced and flexible FFT algorithm that provides an accurate frequency response over the frequency range of interest. Spectral windowing is a process by which the time-history data are segmented, and the frequency response is determined for each segment or window. By averaging the frequency responses from individual window segments, the effect of noise is reduced significantly. In composite windowing, repeated frequency-response determinations are carried out with varying spectral window lengths and these results are then combined using a numerical optimization procedure into a single result. Together, the chirp z-transform and composite window optimization methods produce a frequency-response database of exceptionally high accuracy and resolution over a broad dynamic range for real flight-test data.

When parametric models are required, transfer-function modeling is a rapid and next logical step in the system identification procedure. In the present application, transfer-function modeling was used to evaluate the applicability of quasi-steady (i.e., low-order) models (versus higher-order models that include rotor dynamics), and for determination of the speed damping derivatives (X_u and Y_v). The values of the transfer-function gain, pole locations, and zero locations are determined numerically to provide a best match (in a least squares sense) to the frequency-response data. Transfer-function models are often sufficient end-products of system identification for many applications.

As in the present case for the CH-47 identification project, the end product for many system identification studies is the extraction of state-space or physical model structures. These model structures are formulated directly from the linearized 1st-order differential equations-of-motion as derived from Newton's Second Law. The overall goal of this step is to determine a set of linear 1st-order differential equations constituting a model:

$$M\dot{x} = Fx + Gu \tag{1}$$

$$y = Hx + Ju \tag{2}$$

whose frequency responses match the measured MIMO frequency-response data. Static trim data can also be included in the model structure (as herein) to ensure that the static speed stability derivatives (M_u in this case) are consistent both with the dynamics and trim control behavior.

The complexity of the selected state-space model structure (Eqs. (1)-(2)) depends on the aircraft dynamics and the intended application. For example, most fixed-wing aircraft studies consider the decoupled longitudinal and lateral/directional dynamics – each represented by 3 degrees-of-freedom in 4 state equations. This approach is also satisfactory for characterizing the quasi-steady response of tandem helicopters (e.g., CH-47) and tilt-rotor aircraft (e.g., XV-15, V-22). The quasi-steady assumption models the rotor transient response as a simple equivalent time delay, and thus limits its applicability to low frequencies (below 6 rad/sec in the present case). Improved characterization of the response to higher frequencies as required for high-bandwidth flight control applications generally involves the explicit inclusion of the rotor/inflow equations-of-motion as demonstrated herein. As discussed in Ref. 10 for single rotor helicopters, the longitudinal/lateral-directional dynamics are fully coupled and a satisfactory model for flight control applications involves at least 18 states.

The accuracy of this identified math model is quantified in a cost function, which is the weighted sum of the frequency-response magnitude and phase errors. Initial guesses for the model parameters can be obtained from the transfer-function identification results, a priori estimates based on first principles, or from rapid equation-error regression methods.[14,15] A powerful and highly robust secant optimization algorithm is used to tune the identification parameters in the model structure (e.g., stability and control derivatives, time constants, time delays)

to minimize the identification cost function and thereby drive the model responses to the best match of the flight-test responses. The optimization stops when a minimum cost function value is reached that provides the best choice of identification parameters for the assumed model structure.

At this stage in the process we have achieved a state-space model that best matches the MIMO frequency-response database. Model structure determination finds the model that matches the test data with minimum model redundancy— thereby ensuring that the identified parameters are reliable and retain their physical meaning. The basis for this step is a sensitivity analysis to determine the accuracy and correlation of the parameters that have been identified. The key metrics for this study are the normalized Insensitivities and Cramer-Rao bounds, the latter being a good estimate of parameter accuracy. The sensitivity analysis can show, for example, that certain parameters are known accurately and should be retained in the model, while others have to be discarded because it is impossible to determine or isolate their values due to parameter correlation. Model structure determination, sensitivity analysis, and model reconvergence constitute an iterative loop that refines the structure of the model to ensure that it is both physically appropriate and accurate to within specified error bounds.

With the completion of the model identification in the frequency-domain, it is necessary to verify that the model has good predictive capability and robustness to input shape in the time-domain. For this, we would like to see an accurate and direct comparison of predicted and measured time-responses to measured control-inputs that are completely different in character from those used in the identification. For example, if flight-test data from frequency-sweep inputs were used for the identification, then data from step or multi-step inputs might be used for verification. Evaluating the predictive accuracy for various input amplitudes is useful for assessing the acceptability of the identified linear model. Once the model has been verified, it can be used in the various applications shown.

There are eight important features of the Frequency-Response Identification Method that make it especially well suited to system identification of flight vehicle dynamics from flight-test data:

1) Unbiased frequency-response estimates when flight data contains process and output measurement noise
2) Access to the coherence function as an unbiased measure of nonparametric identification accuracy and system response linearity
3) The wealth of knowledge concerning appropriate model structure provided by the nonparametric identification results
4) Frequency ranges selected individually for each input/output pair to include only accurate data
5) Direct and accurate identification of time delays
6) Elimination of biases and reference shifts as identification parameters
7) Significant improvement in computational efficiency
8) Identification of systems with unstable dynamics

These features are discussed in greater detail in Ref. 10 and many are demonstrated in the CH-47 study herein.

III.   Instrumentation and Flight-Test Data Reduction

A. Aircraft Instrumentation

The test aircraft was instrumented with an Airborne Data Acquisition System (ADAS) that performed the following four data collection functions:

1) Recording of all bus traffic from selected data busses
2) Bus monitoring and placement of selected parameters into the Pulse Code Modulation (PCM) stream for real-time telemetry or post-flight analysis
3) Recording of all transducer data
4) Ethernet data recording

All sensor signals were connected to a Remote Multiplexer Unit (RMU) that conditioned and combined the data channels into a single PCM stream. This final data stream is recorded by the onboard Heim recorder permitting post flight processing of the data.

Aircraft state data was recorded from the onboard Air Data Computer (ADC) and Embedded Global Positioning System (GPS)/Inertial Navigation System (INS) (EGI) from both Channels 1 and 2. In addition, an instrumentation data boom assembly was installed on the nose of the helicopter to measure angle-of-attack, sideslip angle, airspeed, and altitude. The ELA commands and positions were recorded for both channels from FCC1 and FCC2 respectively. Each ILCA was also instrumented with a Linear Variable Differential Transducer (LVDT) at the primary boost actuator to get an accurate measure at the ILCA of the pilot's control input.

B. Signal Processing and Reconstruction

The time history signals used in the signal processing and reconstruction were taken from the PCM data stream recorded on the aircraft's on-board Heim recorder. The time histories were interpolated to 125 Hz to correct for variations in the sample time.

The inputs to the dynamic model are at the output of the mechanical mixer that combines piloted inputs and the Stability Augmentation System (SAS) inputs. At this point, the SAS only shapes the excitation input and is not part of the model. This input choice allows the bare-airframe model to be identified with the stability augmentation system on. The control inputs to the mixer were not instrumented, so the four mixer inputs were reconstructed using measurements upstream of the mixer. A block diagram of the reconstruction of the pitch-mixer input (δ_{LON}) is shown in Figure 8. The gains were obtained from mechanical drawings of the control system, and measurements taken from actuator linkages by maintenance technicians. This diagram is representative of the roll, yaw and collective reconstructions (mechanical gains and conversions differ, and collective does not contain SAS actuators). The reconstruction of the pitch mixer input was verified using data from ground tests. This data set included eight static records of different longitudinal stick positions (recorded using string-pots) with both stability augmentation actuators at 0% and independent static measurements at the pitch-mixer input using a mechanical scale affixed to the input linkage; no pitch-mixer input dynamic data were recorded— making it impossible to quantify hysteresis or other dynamic effects in the linkages. Moreover, no static or dynamic data were available to verify reconstructions of the roll, yaw, or heave mixing-unit inputs.
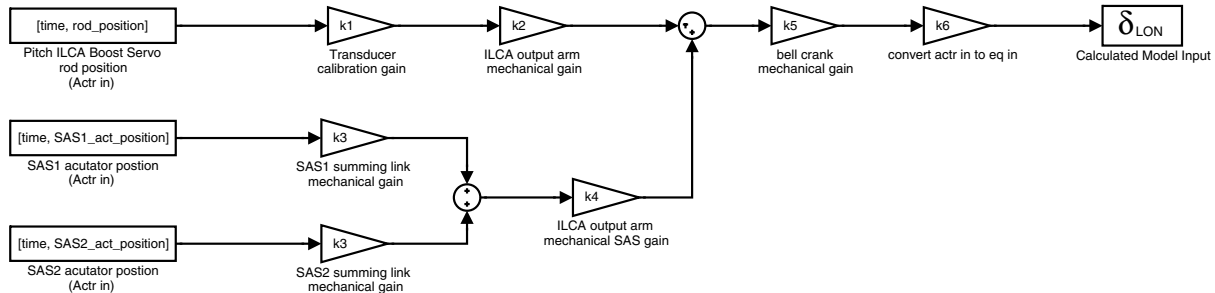

Figure 8. Pitch mixer input reconstruction from upstream control positions.

C. Data Consistency

The kinematic relationships between various measurements can be used to verify that the measurements are kinematically consistent, which is a necessary precursor for system identification analysis. As mentioned earlier in Sec. II, the software tool SMACK was used for analysis of kinematic consistency, data reconstruction, and signal transfer to the center-of-gravity. If the data is kinematically consistent, the SMACK-reconstructed estimate of the signal and the measured signal should be nearly identical.
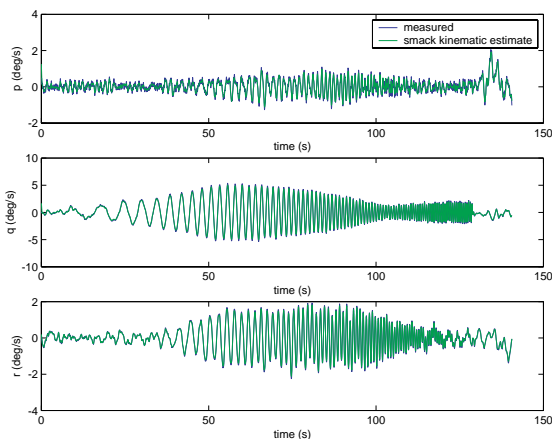

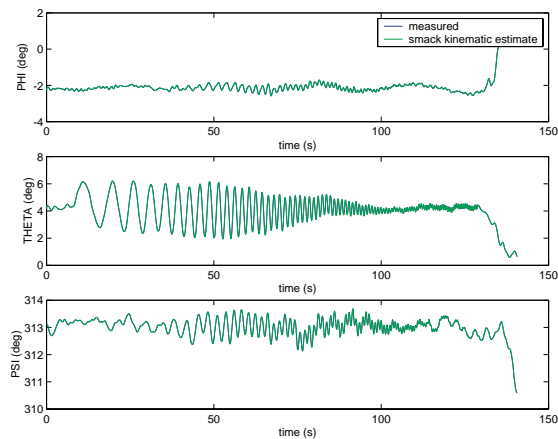**Figure 9. Data consistency for angular rate measurements at hover.**

Figure 10. Data consistency for angular attitude measurements at hover.

American Institute of Aeronautics and Astronautics

The results of the kinematic data consistency analysis for a longitudinal manual sweep at the HGW (~48,000 lbs) hover condition are shown in Figure 9-Figure 12. Figure 9 and Figure 10 indicate that the angular rate and attitude measurements have good kinematic consistency.

Once the accelerations were corrected to the center-of-gravity location from the sensor location, the accelerations demonstrated good kinematic consistency as seen in Figure 11. The velocities are also kinematically consistent as shown in Figure 12.
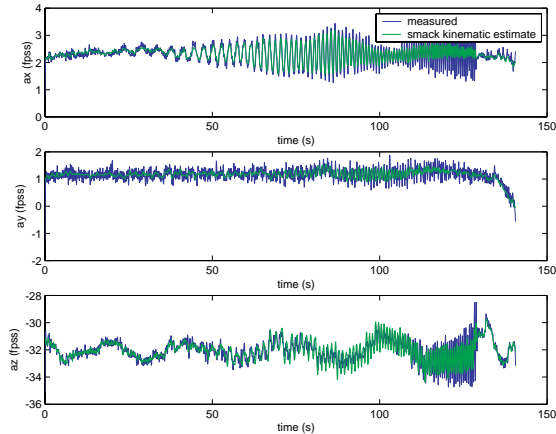

Figure 11. Data consistency for accelerations at hover.
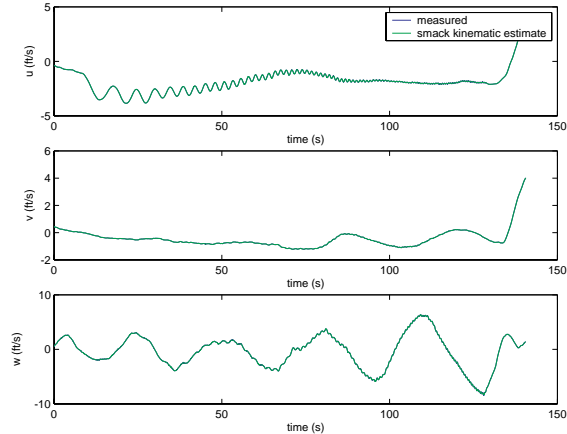
Figure 12. Data consistency for velocities at hover.

IV. Quasi-Steady Model Formulation

The helicopter is modeled as a rigid body, assuming symmetry about the X-Z plane, with the incorporation of equivalent time delays to represent unmodeled rotor dynamics. The linear and angular accelerations are referenced to the helicopter body-axis coordinate system as shown in Figure 13.
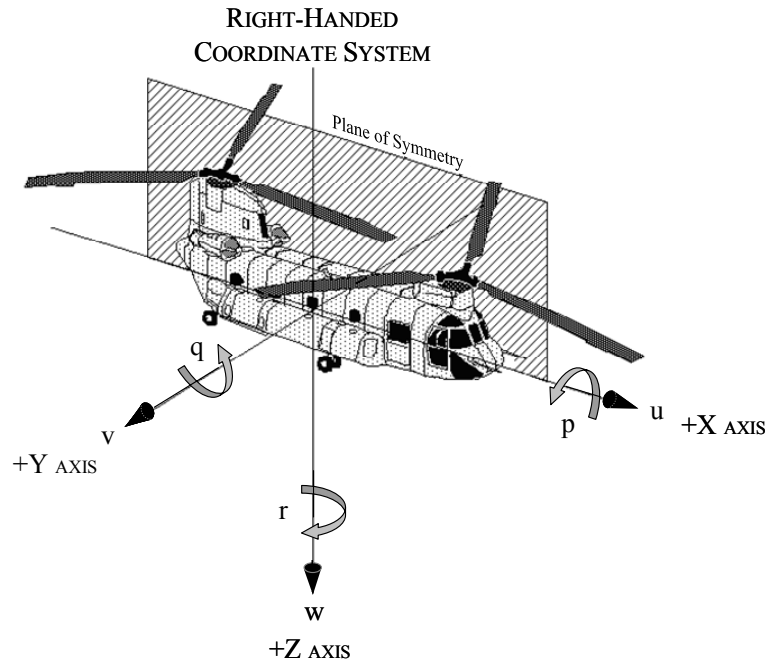

Figure 13. Helicopter body-axis coordinate system.

A. Selection of Frequency Responses used in the Quasi-Steady Model Identification

The frequency responses for the longitudinal/heave dynamics are identified from the kinematically consistent frequency sweep data using CIFER® as described in Sec. II. The body-axis velocity-derivative signals $\dot{u}$ and $\dot{w}$ are useful for state-space model identification and were reconstructed using the kinematic relationships shown in Eq. (3) and Eq. (4).

$$\dot{u} = a_x - g\theta - qw_0 + rv_0 \tag{3}$$

$$\dot{w} = a_z - pv_0 + qu_0 \tag{4}$$

These reconstructed velocity derivatives were used in the identification rather than the velocity signals generated from the Embedded GPS/INS, which exhibited poor coherence.

The accuracy of each frequency response was assessed with the coherence function.[16] Coherence (γ_{xy}^2) is a measure of the quality of the frequency content of a frequency response. Coherence values greater than 0.6 are considered acceptable. It is desirable that the on-axis bare-airframe responses have coherence greater than 0.6 in the range of ~0.1-10 rad/sec for the system identification of a quasi-steady model. Table 2 gives the regions of acceptable coherence for the bare-airframe frequency responses at the HGW hover condition.

Note that a_z and $\dot{w}$ are nearly the same at hover. The quality of the longitudinal/heave frequency responses is acceptable for purposes of system identification because there is good coherence for the on-axis responses over the frequencies of interest for flight dynamics and control (0.1-10 rad/sec).

B. System Identification

1. Quasi-Steady Model Structure

The model structure for the state-space identification was chosen based on the frequency responses that were determined from flight data. The level of coupling was determined by examining the coherence of the off-axes responses. High coherence indicates a coupled response, whereas a low coherence indicates that the output in question was not excited by the control input. The frequency

Table 2. Coherence for longitudinal/heave responses.

Response	δ_{LON}	δ_{COL}
q	0.25 – 10 rad/sec	none
θ	0.25-8 rad/sec	none
a_x	0.15-10 rad/sec	0.25-9 rad/sec
a_z (or $\dot{w}$)	none	0.15-10 rad/sec
$\dot{u}$	0.2-10 rad/sec	0.8-9 rad/sec

responses between longitudinal/heave commands and lateral/directional responses were of poor coherence, indicating that there is little coupling between these axes. Likewise, the frequency responses for lateral/directional commands and longitudinal/heave outputs also had poor coherence. Although the longitudinal cyclic input results in a torque split between the forward and aft rotors, which creates a yaw response, this coupling was not included in the model due to the low magnitude of this response. Therefore, the assumption of decoupled lateral/directional and longitudinal/heave dynamics was sufficient. This is consistent with the symmetric configuration of the tandem-rotor helicopter. Similar decoupling is seen in the XV-15 tilt-rotor.[17]

Dynamic inflow in the collective responses is not included in the quasi-steady model, thereby restricting the frequency range of model fit for the vertical responses to the region near cross-over (0.2-3 rad/sec) where dynamic inflow does not have a large effect. A rotor-on-rotor torque mode in the longitudinal response was observed at ~7 rad/sec. This mode was not included in the quasi-steady model, thereby restricting the frequency range of fit to 6 rad/sec. The structure of the longitudinal/heave model is shown below:

$$M\dot{x} = Fx + Gu \tag{5}$$

$$x = \begin{bmatrix} u & w & q & \theta \end{bmatrix}^T \tag{6}$$

$$u = \begin{bmatrix} \delta_{LON} & \delta_{COL} \end{bmatrix}^T \tag{7}$$

$$F = \begin{bmatrix} X_u & X_w & X_q & -g \\ Z_u & Z_w & Z_q & 0 \\ M_u & M_w & M_q & 0 \\ 0 & 0 & 1 & 0 \end{bmatrix} \text{ and } G = \begin{bmatrix} X_{\delta_{LON}} & X_{\delta_{COL}} \\ Z_{\delta_{LON}} & Z_{\delta_{COL}} \\ M_{\delta_{LON}} & M_{\delta_{COL}} \\ 0 & 0 \end{bmatrix} \qquad (8), (9)$$

Some stability and control derivatives in the above model structure were eliminated by analysis of the frequency-response table of acceptable coherence (Table 2). The coherence for the responses q/δ_{COL} or a_z/δ_{LON} is essentially zero, which indicates that there is no response for these input to output pairs. Therefore, the control derivatives for pitching moment and vertical velocity ($M_{\delta_{COL}}$ and $Z_{\delta_{LON}}$) that correspond to these responses should be eliminated (set to zero). The pitching moment derivative corresponding to the on-axis response to collective $(w), M_w$, should also be eliminated. The vertical force derivatives that correspond to the on-axis response to longitudinal cyclic (u, q), Z_u and Z_q should also be eliminated. This method of model reduction based on the frequency-response table is described in the textbook by Tischler and Remple (Ref. 10).

2. Identification Results

The 3-DOF longitudinal state-space model was determined using the CIFER® tool DERIVID (Sec. II). This tool was used to fit a state-space model to the frequency responses determined from the frequency-sweep flight data. The initial estimates for the stability derivatives were taken from a 6-DOF quasi-steady low-order simulation model of the tandem-rotor helicopter.

The longitudinal speed-damping derivative (X_u) was isolated using the approximation shown in Eq. (10).

$$\dot{u} = X_u u - g\theta \qquad (10)$$

Then by performing a Laplace transform, the equation becomes:

$$\frac{\dot{u}}{q} = \frac{-g}{s - X_u} \qquad (11)$$

This approximation is valid at low frequency (0.2-2 rad/sec). A model of the form of Eq. (11) was identified from the frequency-response $\dot{u}/q$ between 0.2-2 rad/sec using transfer-function fitting (refer to Sec. II for more details). The resulting value of X_u was then fixed in the state-space model.

Although the measurements were corrected to a point near the true center-of-gravity in the SMACK analysis of Sec. III.C, the exact center-of-gravity was unknown. Identification of a vertical center-of-gravity offset (from the estimated center-of-gravity) was implemented in order to correct the acceleration and velocity values to the true center-of-gravity location. The relationship between the measured velocity and the velocity at the center-of-gravity is represented by Eq. (12), which is implemented within the system identification by the **M**-matrix.

$$0 = \dot{u}_m - \dot{u}_{cg} - \dot{q}Z_{offset} \qquad (12)$$

Table 3 gives the identified vertical center-of-gravity offset. After the correction is included, the stability derivatives reflect the dynamics at the identified center-of-gravity location. The vertical center-of-gravity offset

Table 3. M-matrix for quasi-steady model.

Parameter	Value	Cramer-Rao (%)	Insensitivity (%)
Z_{offset}	0.7879	30.47	8.034

represents a discrepancy between the vertical position of the center-of-gravity and the point to which the velocities and accelerations were corrected from the EGI location. This offset is small, 0.7879 feet from the nominal center-of-gravity, but its inclusion improves the system identification. Table 4 shows the identified F-matrix.

Table 4. F-matrix for quasi-steady model.

Parameter	Value	Cramer-Rao (%)	Insensitivity (%)
X_u (1/sec)	-0.01890[*]	N/A	N/A
X_w (1/sec)	7.741e-3	27.02	13.26
X_q (ft/sec)	0[†]	N/A	N/A
Z_u (1/sec)	0[†]	N/A	N/A
Z_w (1/sec)	-0.09929	17.48	8.364
Z_q (ft/sec)	0[†]	N/A	N/A
M_u (1/(sec-ft))	0.01672	6.518	1.690
M_w (1/(sec-ft))	0[†]	N/A	N/A
M_q (1/sec)	-1.306	7.213	1.751

[*] *fixed derivative*
[†] *eliminated during model structure determination*

The stability derivative X_q was eliminated during model structure reduction (Sec. II), due to high insensitivity. Table 4 indicates that the stability derivatives have good accuracy as shown by the low Cramer-Rao bounds and low insensitivity.

Table 5 gives the identified control derivatives and time delays. The time delays are used to account for un-modeled rotor dynamics. The control derivatives and time delays have good theoretical accuracy indicated by the low Cramer-Rao bounds and low insensitivities. The equivalent time delay τ_{COL} was identified with a negative value due to the lead caused by dynamic inflow. Since a negative time delay has no physical meaning, it was eliminated.

Table 5. G-matrix for quasi-steady model.

Parameter	Value	Cramer-Rao (%)	Insensitivity (%)
$X_{\delta_{LON}}$ (ft/sec^2)/in	0.8852	11.22	2.944
$X_{\delta_{COL}}$ (ft/sec^2)/in	0.5686	3.121	1.530
$Z_{\delta_{LON}}$ (ft/sec^2)/in	0[†]	N/A	N/A
$Z_{\delta_{COL}}$ (ft/sec^2)/in	-7.233	3.924	1.868
$M_{\delta_{LON}}$ (1/sec^2)/in	0.5159	3.228	1.207
$M_{\delta_{COL}}$ (1/sec^2)/in	0[†]	N/A	N/A
τ_{LON} (sec)	0.07595	13.19	5.433
τ_{COL} (sec)	0[†]	N/A	N/A

[†] *eliminated during model structure determination*

Table 6 displays the comparative fit of the models to the flight data with a cost function. An average cost below 100 is acceptable. Table 6 shows that the identified state-space model meets the requirement. The graphical overlays of the model against the flight data (and hybrid-model) will be discussed in Sec. V.D.

A common problem in system identification of rotorcraft at hover is that the sign of M_u that results from matching the dynamic response data is not consistent with the trim data. Trim control data can be used to constrain the M_u stability derivative to achieve both a good dynamic and static model. In this case, it was determined that the constraint was not needed because the derivative as identified from the dynamic response data showed the correct sign (positive), without the constraint. However, the trim relationship was used to check the sign and magnitude of the identified M_u derivative. This relationship is given in Eq. (13):

Table 6. Costs for quasi-steady model.

Transfer Function	Cost
$\dot{u}/\delta_{LON}$	181.1
q/δ_{LON}	22.4
a_x/δ_{LON}	109.2
θ/δ_{LON}	166.3
$\dot{u}/\delta_{COL}$	40.0
a_z/δ_{COL}	16.5
a_x/δ_{COL}	31.5
Average	81.0

$$M_u = -\left\{ M_{\delta_{LON}} \left(\frac{\Delta\delta_{LON}}{\Delta u} \right) \right\} \tag{13}$$

From trim flight data at 5-knot perturbations around hover, it was determined that:

$$\frac{\Delta\delta_{LON}}{\Delta u} = -0.0168 \ \text{in/(ft/sec)} \tag{14}$$

Now, M_u can be calculated with Eq. (13) and Eq. (14):

$$M_u = -\left\{ M_{\delta_{LON}} \left(\frac{\Delta\delta_{LON}}{\Delta u} \right) \right\} = -0.5159(-0.0168) = 0.0087 \tag{15}$$

This calculated value of M_u is similar to the identified value given in Table 4 ($M_u = 0.01672$). Although the identified value of M_u is larger (by a factor of ~2), it is of the appropriate sign and rough order of magnitude. This indicates that the identification of M_u is reasonably consistent with trim data.

3. Eigenvalues for the Quasi-Steady Model

The eigenvalues that result from the identification are given in Table 7. There are two left-half-plane eigenvalues and a pair of complex poles in the right half plane. The complex poles at a frequency of 0.59 rad/sec (Eigenvalues 2 and 3) are associated with a lightly unstable pitch phugoid mode. There is stable heave mode at low frequency (Eigenvalue 1) which is consistent with the value of Z_w. The left-half-plane eigenvalue at 1.5 rad/sec (Eigenvalue 4) is the stable pitch-damping mode, which is related to the value of M_q.

Table 7. Eigenvalues of $\mathbf{M}^{-1}\mathbf{F}$ for the quasi-steady model at hover, HGW.

Eigenvalue	Real	Imaginary	Zeta (ζ)	Omega (ω_n) (rad/sec)	Mode
1	-0.9928e-01	0.0000	0.0000	0.0000	Heave
2	0.1059	0.5822	-0.1789	0.5918	Phugoid
3	0.1059	-0.5822	-0.1789	0.5918	Phugoid
4	-1.5370	0.0000	0.0000	0.0000	Pitch-damping

V. Higher-Order Dynamics

As operational mission needs increasingly demand improved handling qualities for safe operations within a DVE, and performance requirements become more stringent as a result, future helicopter flight control systems will most likely employ high-gain, high-authority designs to meet these challenges.

For some designs, using classical SISO design methods, neglecting the presence of higher-order dynamics could result in instabilities due to rotor-fuselage coupling. In addition, higher-bandwidth designs increase the likelihood that rotor dynamics will couple with the control system dynamics, thereby creating closed-loop instabilities.

Therefore, the more accurately the identified state-space model matches the behavior of the real aircraft, the more robust the control design can be made across the operational envelope. With this understanding, system identification requirements were developed for high-bandwidth flight control designs.[18] One of the requirements developed in Ref. 18, is that in order to achieve a robust control system design, the model must be accurate over a frequency range encompassing the intended crossover frequency. In order to determine this frequency range for model validity, one must consider dynamic modes near the crossover frequency. As a general rule, dynamic modes with frequencies within 0.3-3.0 times the crossover frequency will contribute significantly to the closed-loop response; therefore, the model must be accurate over this same range.

For the present case then, the state-space model should be valid over the frequency range of approximately 0.9-9.0 rad/sec due to the proximity of the rotor-on-rotor torque mode to the longitudinal axis gain crossover frequency. The goal of the higher-order modeling was to improve the frequency-domain match over this frequency range.

A. Inflow-Coning Dynamics

During a transient maneuver, unsteady aerodynamic forces cause the inflow through the rotor system to vary from that which is produced during steady level flight. This variation results in a change to the rotor system forces and moments, and therefore affects the rotor flapping response. Dynamic inflow theory seeks to globally model this unsteady aerodynamic effect following sudden changes in rotor blade pitch angle. A good review of dynamic inflow, including many excellent citations dealing with its affect upon the vertical response of the helicopter, is given by Gaonkar and Peters.[19] The vertical response of the helicopter is dominated by three primary effects: heave damping, dynamic inflow, and rotor coning dynamics— each dominating in a different frequency range.

The vertical response to the thrust control lever (i.e., collective), a_z / δ_{COL}, is dominated at low frequencies (up to 1 rad/sec) by the first-order heave mode. Typical values of heave damping are $Z_w = -0.1$; beyond this frequency range its influence becomes negligible. In the mid-frequency region, from about 1 to 12 rad/sec, the vertical response is dominated by the lead effect caused by dynamic inflow; and at higher frequencies, above 20 rad/sec, the vertical response is dominated by rotor coning dynamics. Looking at the $\dot{w}/\delta_{COL}$ response in Figure 20, beginning around 2 rad/sec and continuing out to 12 rad/sec, one can clearly see the lead effect of the dynamic inflow causing an approximate 7 dB increase in magnitude, as well as its associated phase delay; thus leading to the need to include an equivalent time delay in the model structure.

1. Incorporation of Inflow-Coning Dynamics in the Vertical Axis

Chen and Hindson[20] developed several versions of equations-of-motion for various conditions of the coupled heave-inflow-coning dynamics for a single rotor helicopter. In Ref. 9, simplified forms of these equations were used in the SH-2G hybrid identification model and adopted herein. For this tandem-rotor system identification, these equations-of-motion were applied twice— written for the forward and rear rotors neglecting hinge offset and aircraft heave motion. In the vertical axis, the model structure was further simplified by assuming the inflow-coning dynamics were the same at both rotors (i.e., neglecting differences in shaft incidence angles, moment arms, and

American Institute of Aeronautics and Astronautics

load-sharing). Furthermore, rotor-on-rotor aerodynamic interference effects were not directly modeled and will be discussed later. Because the tandem-rotor helicopter is unique in that longitudinal cyclic inputs generate differential collective pitch, as described earlier (i.e., the rotor only sees "collective input" and does not discriminate whether that collective input came from the thrust lever or longitudinal stick), the equations-of-motion were modified to include the additional collective contribution made by longitudinal differential collective pitch. In the notation we distinguish the forward and rear rotor dynamics with the subscripts "F" and "R" respectively. Therefore, the dynamic inflow may be written for each rotor as:

$$
\dot{\upsilon}_F = \underbrace{\left[\frac{-75\,\pi\,\Omega}{32} \left(\overline{v}_0 + \frac{a\,\sigma}{16} \right) C_0 \right]}_{A_{\upsilon_F}} \upsilon_F + \underbrace{\left[\frac{-25\,\pi\,\Omega\,R}{32} \left(\overline{v}_0 + \frac{a\,\sigma}{8} \right) C_0 \right]}_{A_{\dot{\beta}_{0F}}} \dot{\beta}_{0F} + \dots
$$
$$
\dots + \underbrace{\left[\frac{25\,\pi\,\Omega^2\,R}{32} \left(\frac{a\,\sigma}{8} \right) C_0 \right]}_{A_{\delta_{COL}}} K_\theta\, \delta_{COL} + \underbrace{\left[\frac{25\,\pi\,\Omega^2\,R}{32} \left(\frac{a\,\sigma}{8} \right) C_0 \right]}_{A_{\delta_{LON}}} K_{DCP}\, \delta_{LON}
$$

(16)

and,

$$
\dot{\upsilon}_R = \underbrace{\left[\frac{-75\,\pi\,\Omega}{32} \left(\overline{v}_0 + \frac{a\,\sigma}{16} \right) C_0 \right]}_{A_{\upsilon_R}} \upsilon_R + \underbrace{\left[\frac{-25\,\pi\,\Omega\,R}{32} \left(\overline{v}_0 + \frac{a\,\sigma}{8} \right) C_0 \right]}_{A_{\dot{\beta}_{0R}}} \dot{\beta}_{0R} + \dots
$$
$$
\dots + \left[\frac{25\,\pi\,\Omega^2\,R}{32} \left(\frac{a\,\sigma}{8} \right) C_0 \right] K_\theta\, \delta_{COL} - \left[\frac{25\,\pi\,\Omega^2\,R}{32} \left(\frac{a\,\sigma}{8} \right) C_0 \right] K_{DCP}\, \delta_{LON}
$$

(17)

The control gains K_θ and K_{DCP} transform collective and longitudinal control inputs into degrees of rotor blade pitch, respectively, and have units of deg/eq-in (converted to rad/eq-in for consistency with the model structure). These gains were set as free parameters during the identification process. The Carpenter-Fridovich dynamic inflow model factor ($C_0 = 0.639$) was used for the hybrid model formulation, as it provided slightly better results.

The frequency sweep inputs were approximately from 0.3 to 12.5 rad/sec, and therefore do not contain the dynamics associated with rotor coning which would occur around 24 rad/sec. However, the coefficients can be calculated and set as fixed parameters during the identification process. From Ref. 20, the coning dynamics are expressed as a second-order differential equation and are written for each rotor as follows:

$$
\ddot{\beta}_{0F} = \underbrace{\left(\frac{-\Omega\,\gamma}{8} \right)}_{B_{\dot{\beta}_{0F}}} \dot{\beta}_{0F} + \underbrace{\left(-\Omega^2 \right)}_{B_{\beta_{0F}}} \beta_{0F} + \underbrace{\left(\frac{-\Omega\,\gamma}{6\,R} \right)}_{B_{\upsilon_F}} \upsilon_F + \underbrace{\left(\frac{\Omega^2\,\gamma}{8} \right)}_{B_{\delta_{COL}}} K_\theta\, \delta_{COL} + \underbrace{\left(\frac{\Omega^2\,\gamma}{8} \right)}_{B_{\delta_{LON}}} K_{DCP}\, \delta_{LON}
$$

(18)

and,

$$
\ddot{\beta}_{0R} = \underbrace{\left(\frac{-\Omega\,\gamma}{8} \right)}_{B_{\dot{\beta}_{0R}}} \dot{\beta}_{0R} + \underbrace{\left(-\Omega^2 \right)}_{B_{\beta_{0R}}} \beta_{0R} + \underbrace{\left(\frac{-\Omega\,\gamma}{6\,R} \right)}_{B_{\upsilon_R}} \upsilon_R + \left(\frac{\Omega^2\,\gamma}{8} \right) K_\theta\, \delta_{COL} - \left(\frac{\Omega^2\,\gamma}{8} \right) K_{DCP}\, \delta_{LON}
$$

(19)

resulting in additional states for coning angle β_0 and coning rate $\dot{\beta}_0$ for each rotor.

The inflow-coning dynamics are coupled to the fuselage through the thrust coefficient C_T and aircraft mass m, which take the place of the quasi-steady control derivative $Z_{\delta_{COL}}$. This results in the hybrid model structure for the vertical dynamics as given in Eq. (20).

$$\dot{w} = Z_u u + Z_w w + Z_q q + \left(\frac{-\rho \pi R^2 (\Omega R)^2}{m} \right) \widetilde{C}_{T_F} + \left(\frac{-\rho \pi R^2 (\Omega R)^2}{m} \right) \widetilde{C}_{T_R} + Z_{\delta_{LON}} \delta_{LON} \tag{20}$$

However, Ref. 20 defines the thrust coefficient perturbation as:

$$C_0 \widetilde{C}_T = \left(\frac{128}{75 \pi \Omega^2 R} \right) \dot{\upsilon} + \left(\frac{4 \overline{v}_0}{\Omega R} C_0 \right) \upsilon + \left(\frac{4 \overline{v}_0}{3 \Omega} C_0 \right) \dot{\beta}_0 \tag{21}$$

Substituting the expression for dynamic inflow (without rotor subscripts) given in Eq. (16) into Eq. (21) yields the following perturbation equation for the thrust coefficient:

$$\widetilde{C}_T = \left(\frac{-a \sigma}{4 \Omega R} \right) \upsilon + \left(\frac{-a \sigma}{6 \Omega} \right) \dot{\beta}_0 + \left(\frac{a \sigma}{6} \right) K_\theta \, \delta_{COL} \pm \left(\frac{a \sigma}{6} \right) K_{DCP} \, \delta_{LON} \tag{22}$$

Notice how the dynamic inflow model factor C_0 cancels out and therefore has no direct effect in the vertical dynamics. Substituting Eq. (22) into Eq. (20) yields the final hybrid model structure for the vertical dynamics:

$$\dot{w} = Z_u u + Z_w w + Z_q q + \underbrace{\left(\frac{\rho a \sigma \pi \Omega R^3}{4 \cdot m} \right)}_{Z_{\upsilon_F}} \upsilon_F + \underbrace{\left(\frac{\rho a \sigma \pi \Omega R^4}{6 \cdot m} \right)}_{Z_{\dot{\beta}_{0F}}} \dot{\beta}_{0F} + \underbrace{\left(\frac{\rho a \sigma \pi \Omega R^3}{4 \cdot m} \right)}_{Z_{\upsilon_R}} \upsilon_R + \dots$$

$$\dots + \underbrace{\left(\frac{\rho a \sigma \pi \Omega R^4}{6 \cdot m} \right)}_{Z_{\dot{\beta}_{0R}}} \dot{\beta}_{0R} + \underbrace{2 \left(\frac{-\rho a \sigma \pi \Omega^2 R^4}{6 \cdot m} \right) K_\theta \, \delta_{COL}}_{\hat{Z}_{\delta_{COL}}} + Z_{\delta_{LON}} \, \delta_{LON} \tag{23}$$

For simplicity, it was assumed that both rotors were at the same height (i.e., no stagger) and equally share the weight of the aircraft; resulting in a factor of 2 for the collective control term. Also, notice how the longitudinal differential collective pitch terms have cancelled out— leaving only the quasi-steady longitudinal control derivative $Z_{\delta_{LON}}$ as expected.

2. Incorporation of Inflow-Coning Dynamics in the Longitudinal Axis

The effects of dynamic inflow are also observed in the longitudinal a_x / δ_{COL} frequency response (Figure 19); and although the coherence was poor, the effect was also noticeable in the θ / δ_{COL} frequency response.

A general arrangement of the rotor forces and moments acting upon the helicopter in the longitudinal axis is presented in Figure 14. Recall that the summation of moments in the longitudinal axis is given by:
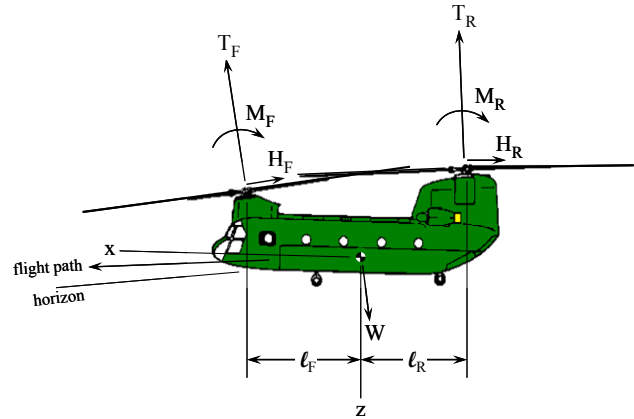

Figure 14. Tandem-rotor longitudinal forces and moments.

$$\sum M = 0: \quad I_{yy} \ddot{\theta} = I_{yy} \dot{q} = 0 \tag{24}$$

Therefore, by multiplying the thrust coefficient perturbation by the moment arm and dividing by the mass moment of inertia, we achieve a simple approximation for the thrust coefficient contribution to pitching moment given by:

$$\left(\frac{\rho \pi R^2 (\Omega R)^2 \ell}{I_{yy}} \right) \widetilde{C}_T = M_{C_T} \widetilde{C}_T = \frac{\Delta T \ell}{I_{yy}} \tag{25}$$

In the hybrid model structure, the thrust coefficient contribution replaces the $M_{\delta_{LON}}$ and $M_{\delta_{COL}}$ control derivatives as shown in Eq. (26). Note that the quasi-steady derivative M_q remains in the model structure for reasons to be discussed later.

$$\dot{q} = M_u u + M_w w + M_q q + M_{C_{T_F}} \widetilde{C}_{T_F} - M_{C_{T_R}} \widetilde{C}_{T_R} \tag{26}$$

Unlike the vertical axis, the effect of different moment arms (i.e., $\ell_F \neq \ell_R$) was included in the parameter constraints for the longitudinal axis. As before, the thrust coefficient perturbation is eliminated via substitution resulting in the final hybrid pitch acceleration equation:

$$\dot{q} = M_u u + M_w w + M_q q + \underbrace{\left(\frac{-\rho a \sigma \pi \Omega R^3 \ell_F}{4 I_{yy}} \right)}_{M_{\upsilon_F}} \upsilon_F + \underbrace{\left(\frac{-\rho a \sigma \pi \Omega R^4 \ell_F}{6 I_{yy}} \right)}_{M_{\dot{\beta}_{0F}}} \dot{\beta}_{0F} + \underbrace{\left(\frac{\rho a \sigma \pi \Omega R^3 \ell_R}{4 I_{yy}} \right)}_{M_{\upsilon_R}} \upsilon_R + \ldots$$

$$\ldots + \underbrace{\left(\frac{\rho a \sigma \pi \Omega R^4 \ell_R}{6 I_{yy}} \right)}_{M_{\dot{\beta}_{0R}}} \dot{\beta}_{0R} + \underbrace{\left[\left(\frac{\rho a \sigma \pi \Omega^2 R^4 \ell_F}{6 I_{yy}} \right) + \left(\frac{\rho a \sigma \pi \Omega^2 R^4 \ell_R}{6 I_{yy}} \right) \right] K_{DCP}}_{\hat{M}_{\delta_{LON}}} \delta_{LON} + \ldots \tag{27}$$

$$\ldots + \underbrace{\left[\left(\frac{\rho a \sigma \pi \Omega^2 R^4 \ell_F}{6 I_{yy}} \right) - \left(\frac{\rho a \sigma \pi \Omega^2 R^4 \ell_R}{6 I_{yy}} \right) \right] K_{\theta}}_{\hat{M}_{\delta_{COL}}} \delta_{COL}$$
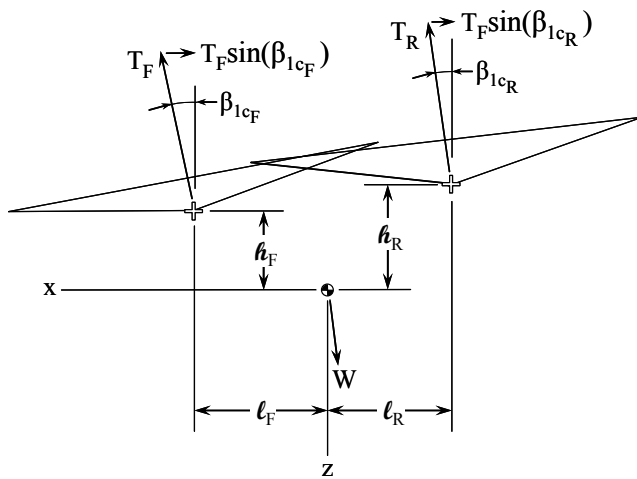

Figure 15. Tandem-rotor longitudinal flapping.

Referring to Figure 15, the effect of dynamic inflow in the quasi-steady $\dot{u}$ acceleration equation is shown to be a function of the TPP longitudinal flapping. To get the linear acceleration contribution for the thrust coefficient, the thrust coefficient contribution in the vertical axis was multiplied by $\sin(\beta_{1c}) \approx \beta_{1c}$ (using the small angle approximation); which results in a nonlinear product of state variables, assuming X_{C_T} is constant, as shown below:

$$\underbrace{\left(\frac{\rho \pi R^2 (\Omega R)^2}{m} \right)}_{X_{C_T}} C_T \beta_{1c} = \frac{T \beta_{1c}}{m} \tag{28}$$

This nonlinear product between C_T and β_{1c} must be linearized before inclusion in the quasi-

steady equation. Chen[21] developed complete equations describing the TPP dynamics for a single rotor helicopter; and in the hybrid identification model structure of Ref. 9, these expressions for TPP flapping are simplified, such that the longitudinal flapping equation is given by:

$$\tau_f \dot{\beta}_{1c} = -\beta_{1c} + Mf_{\beta_{1s}}\beta_{1s} + \tau_f q + Mf_{\delta_{LAT}}\delta_{LAT} + Mf_{\delta_{LON}}\delta_{LON} \tag{29}$$

Although a tandem-rotor is free to flap longitudinally, it is not directly controlled by longitudinal cyclic; rather, it is a secondary effect of longitudinal differential collective pitch and therefore the $Mf_{\delta_{LON}}\delta_{LON}$ term must be dropped from the flapping equation. Further, because the model is decoupled from the lateral/directional axes, the lateral axis terms must also be dropped. This results in a very simplified longitudinal flapping equation driven solely by pitch rate:

$$\tau_f \dot{\beta}_{1c} = -\beta_{1c} + \tau_f q \tag{30}$$

Given this result, it was decided not to further complicate the model structure by including β_{1c} as a state variable; choosing rather to keep the quasi-steady pitch rate term M_q and include an equivalent time delay to represent the flapping time constant τ_f. Linearizing Eq. (28) using the perturbation method about a steady-state hover yields:

$$
\begin{aligned}
f(C_T, \beta_{1c}) &\doteq X_{C_T} C_{T_0} \beta_{1c_0} + X_{C_T} C_{T_0} \Delta\beta_{1c} + X_{C_T} \beta_{1c_0} \Delta C_T + \underbrace{X_{C_T} \Delta C_T \Delta\beta_{1c}}_{negligible \,<<\, 1} \\
&= \underbrace{X_{C_T} C_{T_0} \beta_{1c_0}}_{negligible\ bias} + \underbrace{X_{C_T} C_{T_0} \Delta\beta_{1c}}_{\substack{captured\ by \\ quasi-steady\ terms}} + X_{C_T} \beta_{1c_0} \Delta C_T \\
&= X_{C_T} \beta_{1c_0} \Delta C_T = X_{C_T} \beta_{1c_0} \widetilde{C}_T
\end{aligned}
\tag{31}
$$

The above result is incorporated into the linear acceleration equation for both rotors in lieu of the $X_{\delta_{COL}}$ control derivative. Substituting for $\widetilde{C}_T$, as previously done, the final hybrid-structure for the linear acceleration quasi-steady equation (assuming $\beta_{1c_0} = \beta_{1c_{0\,F}} = \beta_{1c_{0\,R}}$) is:

$$
\begin{aligned}
\dot{u} &= X_u u + X_w w + X_q q + \underbrace{X_{C_T} \beta_{1c_0}\left(\frac{-a\sigma}{4\Omega R}\right) \upsilon_F}_{X_{\upsilon_F}} + \underbrace{X_{C_T} \beta_{1c_0}\left(\frac{-a\sigma}{6\Omega}\right) \dot{\beta}_{0_F}}_{X_{\dot{\beta}_{0_F}}} + \ldots \\
&\ldots + \underbrace{X_{C_T} \beta_{1c_0}\left(\frac{-a\sigma}{4\Omega R}\right) \upsilon_R}_{X_{\upsilon_R}} + \underbrace{X_{C_T} \beta_{1c_0}\left(\frac{-a\sigma}{6\Omega}\right) \dot{\beta}_{0_R}}_{X_{\dot{\beta}_{0_R}}} + \underbrace{X_{C_T} \beta_{1c_0}\left(\frac{a\sigma}{3}\right) K_\theta \delta_{COL}}_{\hat{X}_{\delta_{COL}}} + X_{\delta_{LON}} \delta_{LON}
\end{aligned}
\tag{32}
$$

B. Rotor-on-Rotor Dynamics

As shown in Figure 16, the Chinook's tandem-rotor arrangement overlaps the rotor diameters approximately 34%. This configuration results in a considerable aerodynamic interference between the rotors, and between the rotors and fuselage. The rotor-fuselage interference effect, caused by the downwash of both rotors, is not explicitly accounted for in the model structure.

1. Rotor-on-Rotor Aerodynamic Interference Mode

The individual vortex system generated by each rotor imparts an additional induced velocity on the other rotor.

In an analytical model this is accounted for by using empirically derived interference factors based upon flight-test data. For this system identification, the effect is not explicitly modeled. However, the dynamic inflow effect is clearly present in the data. Therefore, the stability derivatives for the forward and rear inflow state equations were freed in the CIFER[®] identification process in an effort to account for this interference effect; rather than being constrained to the theoretical value.

2. Rotor-on-Rotor Torque Mode

As described in Sec. I.B.1, the forward and rear rotors are coupled together through the drive system. Miller and White,[22] in modeling rotor-fuselage coupling effects for a CH-47B, examined the effects of drive system flexibility on control design and aircraft handling qualities. In Ref. 22, Miller and White describe the combined effects of the two rotors, when considering coupled in-plane/fuselage dynamics, in terms of symmetric and anti-symmetric modes. Symmetric modes result in identical changes to both rotors, while anti-symmetric modes result in changes of opposite sign on the rotors.

The rotor-on-rotor torque mode is therefore an anti-symmetric in-plane mode characterized by the forward rotor lagging while the rear rotor is concurrently leading. The simultaneous lagging-and-leading motion of the rotor system associated with this anti-symmetric mode produces thrust and torque deviations of opposite signs on the two rotors. As a result, fuselage pitching and yawing moments are generated. If the drive system was able to

Figure 16. Tandem-rotor arrangement.

rigidly connect the two rotors, then the rotor-on-rotor torque mode would occur at approximately 8 rad/sec; however, due to drive system flexibility this mode is softened to approximately 6.8 rad/sec.

As shown later in Figure 17 and Figure 18, the rotor-on-rotor torque mode lag-lead effect is clearly seen in the $\dot{u}/\delta_{LON}$, a_x/δ_{LON}, q/δ_{LON}, and θ/δ_{LON} frequency responses at approximately 6.8 rad/sec. The original 3-DOF quasi-steady model is band-limited to 6 rad/sec in the longitudinal axis because it does not model the rotor-on-rotor dynamics. Unfortunately, no drive system parameters (i.e., torque, rotor RPM, etc.) were recorded concurrently with the frequency-domain flight testing; and no attempt was made at incorporating a drive system model into the state-space formulation as it was not needed for the control development effort.

The longitudinal/heave hybrid model was extended to include the rotor-on-rotor torque mode by appending a lag-lead network to the state-space model structure to fit the affected frequency responses. Rather than being incorporated directly into the state-space model structure, the lag-lead network was incorporated as a second order filter using CIFER[®]'s ability to model sensor dynamics. The NAVFIT tool within CIFER[®] was used to determine a second order transfer function fit to the affected frequency responses in the region of 4 to 10 rad/sec. The NAVFIT solution for the q/δ_{LON} frequency response was used as the initial estimate for the rotor-on-rotor torque mode numerator and denominator coefficients. All numerator and denominator sensor coefficients for the affected frequency responses were constrained to achieve a single solution for the lag-lead network used to represent this mode.
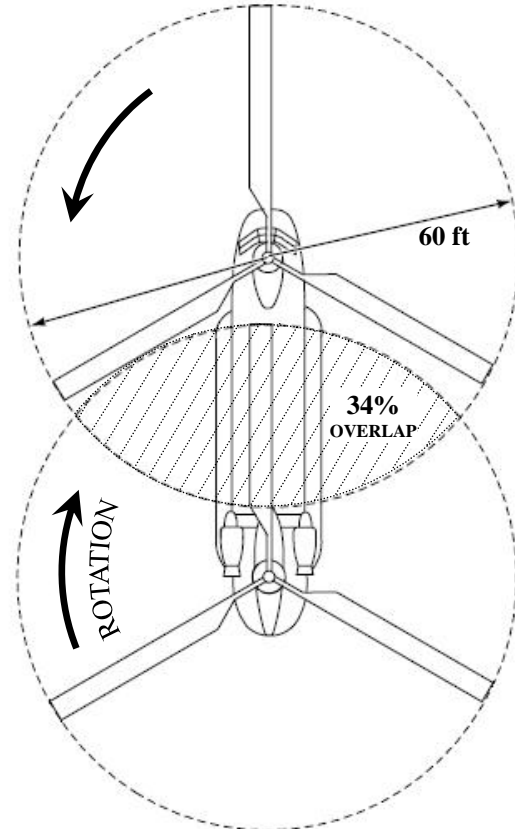
C. Selection of Frequency Responses used in the Higher-Order Hybrid Model Identification

For the higher-order identification, the frequency responses were regenerated from the original data without any additional filtering since data filtering was already performed by the data acquisition system. As a result, the coherence and usable frequency range were slightly improved. During the longitudinal doublet maneuver (shown later in Figure 21), it was observed that there was a vertical velocity response to the longitudinal cyclic control inputs at approximately 9 seconds (see Figure 23). Therefore, the only additional frequency response used in the higher-order identification was $\dot{w}/\delta_{LON}$. In general, the coherence for the $\dot{w}/\delta_{LON}$ response was not good, but there was a useable range from approximately 1 to 2 rad/sec (average coherence of ~0.5). For the higher-order system identification, the frequency range over the region of acceptable coherence is given in Table 8.

Table 8. Frequency range with usable coherence.

Response	δ_{LON}	δ_{COL}
$\dot{u}$	0.15–13 rad/sec	0.8–9 rad/sec
q	0.2–14 rad/sec	none
θ	0.15–10 rad/sec	none
a_x	0.105–13 rad/sec	0.2–9 rad/sec
a_z (or $\dot{w}$)	0.9–2.0 rad/sec	0.105–10 rad/sec

D. System Identification
1. Hybrid-Model Structure

As described in Sec. V.A, the quasi-steady equations are extended using Eq. (23), (27), and (32). In addition, 6 new state equations are added to the state-space model: Eq. (16)-(19), plus two state equations capturing the kinematic relation between coning (β_0) and coning rate ($\dot{\beta}_0$) for each rotor. Whereas the quasi-steady model structure consisted of 4 state variables and 3 degrees-of-freedom for the rigid-body motion, the hybrid model structure consists of 12 state variables: $x = \begin{bmatrix} u & w & q & \theta & \upsilon_F & \upsilon_R & \beta_{0_F} & \beta_{0_R} & \dot{\beta}_{0_F} & \dot{\beta}_{0_R} \end{bmatrix}^T$ *(plus the two pseudo-states associated with the rotor-on-rotor torque mode lag-lead network)*, and 6 degrees-of-freedom: 3-DOF for the rigid-body motion, 1-DOF for the dynamic inflow contribution, 1-DOF for rotor coning, and 1-DOF associated with the in-plane blade motion of the rotor-on-rotor torque mode.

2. Identification Results

The center-of-gravity offset (Z_{offset}) that was determined in the 3-DOF quasi-steady model was fixed at its baseline value for the hybrid model identification. The final values for the stability and control derivatives of the hybrid model structure were determined using the DERIVID tool within CIFER®. The hybrid state-space model was optimized using a minimum frequency of 1 rad/sec for the longitudinal axis and a global maximum frequency of 10 rad/sec. Other minimum frequencies remained as reported in Table 8. However, for comparison with the quasi-steady model, the insensitivity and Cramer-Rao percentages were calculated over the frequency range of approximately 0.1-10 rad/sec.

The stability derivatives for the F-matrix are given in Table 9. Referring to Table 9, the two speed-derivatives X_u and M_u, denoted with an (*), were initially freed during the DERIVID process, but were finally constrained to the baseline quasi-steady values because the variation and reduction in the cost function were insignificant.

Derivatives denoted with a (†) were eliminated during the model structure determination as a result of high insensitivity values.

Derivatives denoted with a (‡) were proportionally constrained to other derivatives due to the underlying physics-based equations. As an example, referring to Eq. (27), notice that the higher-order stability derivatives $M_{\dot{\beta}_{0_F}}$, M_{υ_R}, and $M_{\dot{\beta}_{0_R}}$ are all scalar functions of M_{υ_F} since they share an underlying set of physical parameters. Accordingly then, these derivatives were constrained to M_{υ_F} in order to maintain their physical relationships.

Derivatives denoted with a (§) were constrained to their theoretical values. For example, the coning dynamics, which occur at approximately the 1/rev frequency (~24 rad/sec), are not contained within the frequency sweep data as demonstrated by Table 8; therefore, the stability derivatives for the coning dynamics, expressed in Eq. (18)-(19), were fixed to their theoretical values.

The results for the hybrid-model control derivatives are given in Table 10.

Table 9. F-matrix for higher-order hybrid model.

Parameter	Value	Cramer-Rao (%)	Insensitivity (%)	Parameter	Value	Cramer-Rao (%)	Insensitivity (%)
X_u (1/s)	-0.0189[*]	N/A	N/A	M_{υ_F} (1/(s-ft))	-0.04179	20.29	2.143
X_w (1/s)	6.951e-3	36.29	16.62	$M_{\dot{\beta}_{0_F}}$ (1/s))	-0.8357[‡]	N/A	N/A
X_q (ft/s)	0[†]	N/A	N/A	M_{υ_R} (1/(s-ft))	0.03776[‡]	N/A	N/A
X_{υ_F} (1/s)	-0.03237[‡]	N/A	N/A	$M_{\dot{\beta}_{0_R}}$ (1/s)	0.7552[‡]	N/A	N/A
$X_{\dot{\beta}_{0_F}}$ (ft/s)	-0.6406[‡]	N/A	N/A	A_{υ_F} (1/s)	-9.173	6.89	1.473
X_{υ_R} (1/s)	-0.03237[‡]	N/A	N/A	$A_{\dot{\beta}_{0_F}}$ (ft/s)	-149.0	7.04e-3	6.179
$X_{\dot{\beta}_{0_R}}$ (ft/s)	-0.6406[‡]	N/A	N/A	A_{υ_R} (1/s)	-9.173[‡]	N/A	N/A
Z_u (1/s)	0[†]	N/A	N/A	$A_{\dot{\beta}_{0_R}}$ (ft/s)	-149.0[‡]	N/A	N/A
Z_w (1/s)	-0.1053	16.34	7.445	$B_{\dot{\beta}_{0_F}}$ (1/s)	-26.16[§]	N/A	N/A
Z_q (ft/s)	-6.653	7.41	2.64	$B_{\beta_{0_F}}$ (1/s^2)	-555.2[§]	N/A	N/A
Z_{υ_F} (1/s)	0.4002[§]	N/A	N/A	B_{υ_F} (1/s-ft)	-1.163[§]	N/A	N/A
$Z_{\dot{\beta}_{0_F}}$ (ft/s)	8.004[§]	N/A	N/A	$B_{\dot{\beta}_{0_R}}$ (ft/s)	-26.16[§]	N/A	N/A
Z_{υ_R} (1/s)	0.4002[§]	N/A	N/A	$B_{\beta_{0_R}}$ (1/s^2)	-555.2[§]	N/A	N/A
$Z_{\dot{\beta}_{0_R}}$ (ft/s)	8.400[§]	N/A	N/A	B_{υ_R} (1/s-ft)	-1.163[§]	N/A	N/A
M_u (1/(s-ft))	0.01672[*]	N/A	N/A				
M_w (1/(s-ft))	0[†]	N/A	N/A				
M_q (1/s)	-1.165	9.667	1.885				

[*] *fixed derivative*
[†] *eliminated during model structure determination*
[‡] *constrained to another derivative*
[§] *constrained to theoretical value*

Table 10. G-matrix for higher-order hybrid model.

Parameter	Value	Cramer-Rao (%)	Insensitivity (%)	Parameter	Value	Cramer-Rao (%)	Insensitivity (%)
$X_{\delta_{LON}}$ (ft/s^2)/in	0.7206	10.65	2.985	$\hat{X}_{\delta_{COL}}$ (ft/s^2)/in	0.9810	4.836	1.614
$Z_{\delta_{LON}}$ (ft/s^2)/in	0.9836	10.76	4.134	$\hat{Z}_{\delta_{COL}}$ (ft/s^2)/in	-12.20	4.148	1.505
$\hat{M}_{\delta_{LON}}$ (1/s^2)/in	0.6280	7.009	1.119	$\hat{M}_{\delta_{COL}}$ (1/s^2)/in	0.02786	18.87	5.253
$A_{F\,\delta_{LON}}$ (ft/s^2)/in	27.05[‡]	N/A	N/A	$A_{F\,\delta_{COL}}$ (ft/s^2)/in	52.02[‡]	N/A	N/A
$B_{F\,\delta_{LON}}$ (1/s^2)/in	10.37[‡]	N/A	N/A	$B_{F\,\delta_{COL}}$ (1/s^2)/in	19.94[‡]	N/A	N/A
$A_{R\,\delta_{LON}}$ (ft/s^2)/in	-27.05[‡]	N/A	N/A	$A_{R\,\delta_{COL}}$ (ft/s^2)/in	52.02[‡]	N/A	N/A
$B_{R\,\delta_{LON}}$ (1/s^2)/in	-10.37[‡]	N/A	N/A	$B_{R\,\delta_{COL}}$ (1/s^2)/in	19.94[‡]	N/A	N/A

[‡] *constrained to another derivative*

Referring to Table 10, the control derivative $\hat{X}_{\delta_{COL}}$ was a free parameter. The steady-state coning angle β_{1c_0}, was calculated from the identified value of $\hat{X}_{\delta_{COL}}$ using the relationship shown in Eq. (32).

The $\hat{Z}_{\delta_{COL}}$ control derivative was a free parameter in the DERIVID optimization process. The inflow and coning control derivatives for the collective axis were proportionally constrained to $\hat{Z}_{\delta_{COL}}$ due to underlying physical relationships. The control gain K_θ is calculated from the identified $\hat{Z}_{\delta_{COL}}$ control derivative using the relationship shown in Eq. (23).

The $\hat{M}_{\delta_{LON}}$ derivative was also a free parameter. The inflow and coning control derivatives for the longitudinal axis were proportionally constrained to $\hat{M}_{\delta_{LON}}$ due to underlying physical relationships. The control gain K_{DCP} is calculated from the $\hat{M}_{\delta_{LON}}$ control derivative using Eq. (27).

The values for β_{1c_0}, K_θ, and K_{DCP} were calculated from the CIFER® results and are compared to theoretical values as shown in Table 11.

The large error in K_{DCP} is due to a combination of factors: considering the rotors in isolation (i.e., neglecting rotor-body and rotor-on-rotor aerodynamic interference effects) and uncertainty in the estimate for I_{yy}.

Table 11. Coning and control gain determinations.

Variable	Value	Theoretical Value	Error (%)
β_{1c_0} (rad)	0.0402**	0.0369**	8.94
K_θ (rad/in)	0.03235	0.0325	0.46
K_{DCP} (rad/in)	0.0168	0.0108	55.5

** neglecting blade twist

During the hybrid model structure determination, an equivalent time delay was included for the longitudinal axis (as described earlier to account for longitudinal flapping). In addition, an equivalent time delay was also included for the collective axis; as it was observed to improve the phase curve roll-off in the mid-frequency region due to the effect of dynamic inflow. The CIFER® identified time delays are given in Table 12.

Table 12. Tau-matrix for higher-order hybrid model.

Parameter	Value	Cramer-Rao (%)	Insensitivity (%)
τ_{LON} (sec)	0.04339	17.19	6.722
τ_{COL} (sec)	0.02917	30.86	13.24

As discussed in Sec. V.B.2, the rotor-on-rotor torque mode is modeled as a second-order system given by:

$$\overline{R}(s) = \frac{n_2 s^2 + n_1 s + n_0}{d_2 s^2 + d_1 s + d_0} \qquad (33)$$

During the identification process of fitting the hybrid model in the range of the rotor-on-rotor torque mode for the $\dot{u}/\delta_{LON}$, q/δ_{LON}, a_x/δ_{LON}, θ/δ_{LON} responses, it was observed that the linear acceleration responses and angular accelerations would have resulted in slightly different 2nd order dynamics if each pair had been optimized separately. This anomaly was observed by the Army/Boeing test team when examining short-term linear accelerations resulting from pitch attitude changes; it is suspected that these variations are due to external

Table 13. Rotor-on-rotor torque mode coefficients.

Parameter	Value	Cramer-Rao (%)	Insensitivity (%)
n_2	0.1045	6.974	0.7881
n_1	0.1911	26.64	3.106
n_0	5.970	2.077	0.6011
d_2	0.08205	11.79	1.209
d_1	0.2915	30.08	2.285
d_0	4.554	3.534	0.7632

disturbances. Regardless, the numerator and denominator sensor coefficients were constrained across all four frequency responses to ensure a single lag-lead network was identified representing the rotor-on-rotor torque mode. The coefficients for the rotor-on-rotor torque mode and their theoretical accuracy metrics are given in Table 13.

Table 14 provides a comparison of the cost functions for both models over the frequency range for which each was optimized, as well as over the entire range containing acceptable coherence. As stated earlier, an average cost function below 100 is acceptable to ensure that the model fits well with the frequency-domain flight-test data. The goal of the higher-order model system identification was to extend the quasi-steady model to higher frequencies while improving both the frequency response fit and cost. Over the range of 1-10 rad/sec, for which it was optimized, the hybrid model has an average cost function of 29.0.

Table 14. Comparison of cost function between models.

Transfer Function	Cost (MIN to 6 rad/sec)		Cost (MIN to 10 rad/sec)		Cost (1 to 10 rad/sec)	
	Quasi-steady	Hybrid	Quasi-steady	Hybrid	Quasi-steady	Hybrid
$\dot{u}/\delta_{LON}$	181.1	172.3	185.4	155.5	62.1	17.1
q/δ_{LON}	22.4	9.7	60.3	14.5	60.3	14.5
a_x/δ_{LON}	109.2	111.0	114.3	102.5	88.2	57.5
θ/δ_{LON}	166.3	155.1	149.0	137.3	33.8	12.4
$\dot{w}/\delta_{LON}$	N/A	21.2	N/A	21.2	N/A	21.2
$\dot{u}/\delta_{COL}$	40.0	30.5	180.3	34.0	189.0	22.0
a_z/δ_{COL}	16.5	27.8	131.7	29.9	227.9	35.2
a_x/δ_{COL}	31.5	52.9	96.3	53.2	140.2	52.7
Average	81.0	67.2	117.7	63.6	103.7	29.0

3. Comparison of Frequency-Response Matches to Flight Data and Quasi-Steady Model.

Although each model was optimized across overlapping, yet different frequency ranges, for comparison purposes the two models are overlaid with the flight-test data over the frequency range of approximately 0.1-10 rad/sec. Recall that some frequency responses were truncated around 1 rad/sec due to poor coherence below this frequency. Figure 17-Figure 20 show comparisons of both the quasi-steady and hybrid model to the flight data.

In Figure 17-Figure 18, one can see that both models match well over the frequency range for which each was optimized. For $\dot{u}/\delta_{LON}$ and θ/δ_{LON} the identified models match the flight data well in the magnitude at low and mid-frequencies, but the phase response does not fit as well at low frequency. There is poor coherence at low frequency (where mismatch occurs), indicating that the frequency response from flight data may be distorted due to nonlinearities. DERIVID also de-weights low coherence segments of the frequency response, because the flight data is less accurate here. The combination of possible distortion due to nonlinearities and de-weighting of the data is likely the cause of the mismatch in phase and magnitude at low frequency.

As expected, the hybrid model shows an improved fit to the rotor-on-rotor torque mode around 7 rad/sec in all of the longitudinal responses. Although the hybrid model was optimized from 1-10 rad/sec, the quality of the fit below 1 rad/sec is not significantly worse than the quasi-steady model, which included data between 0.25-6 rad/sec.
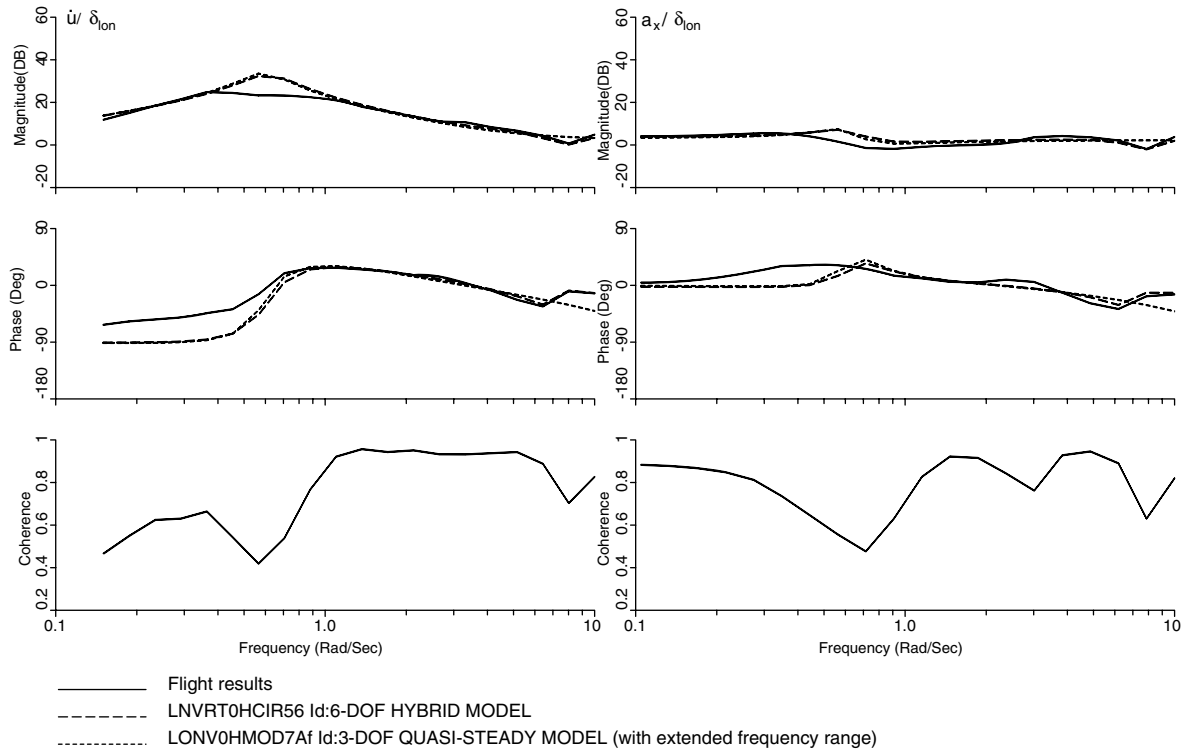
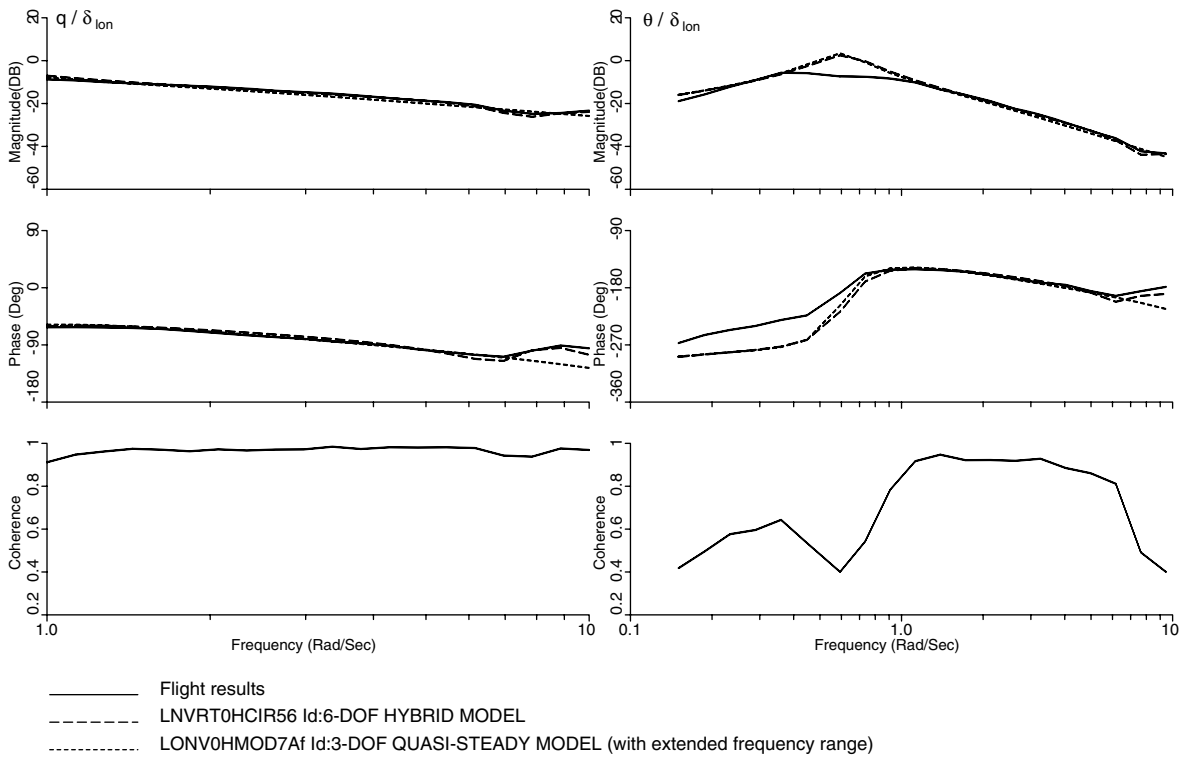**Figure 17. Comparison of quasi-steady and hybrid-model to flight data for $\dot{u}/\delta_{LON}$ and a_x/δ_{LON}.**

Figure 18. Comparison of quasi-steady and hybrid-model to flight data for q/δ_{LON} and θ/δ_{LON}.

American Institute of Aeronautics and Astronautics
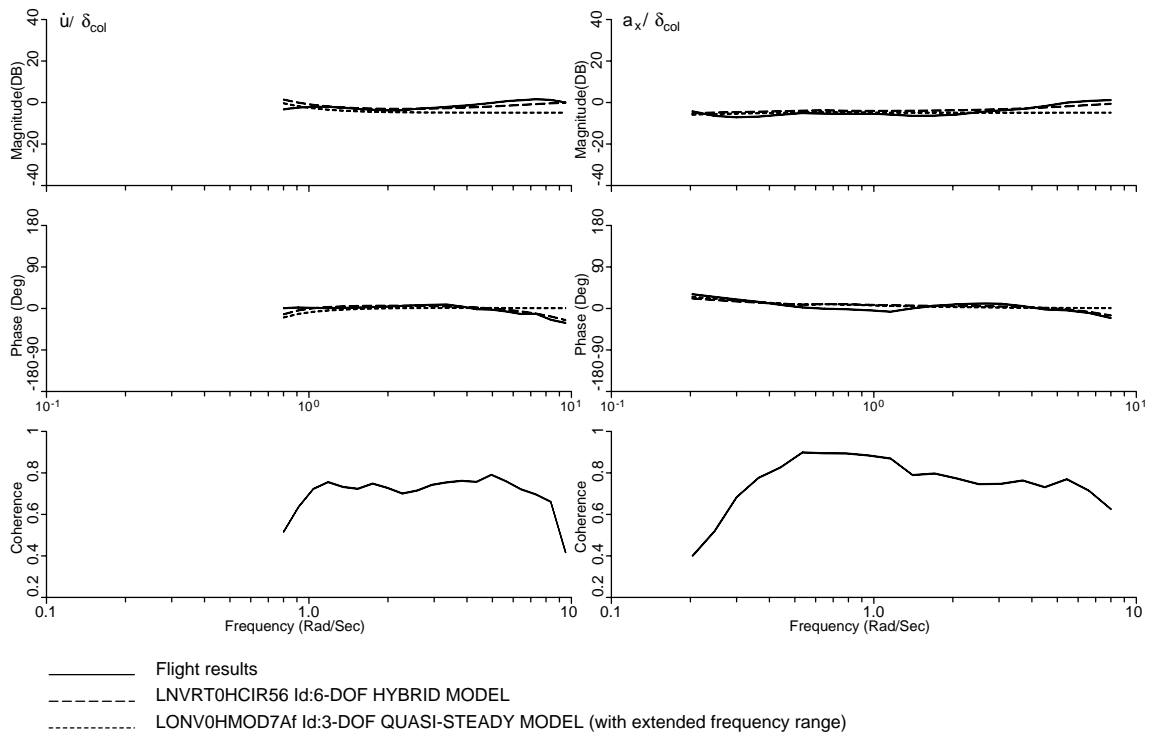
Figure 19. Comparison of quasi-steady and hybrid-model to flight data for $\dot{u}/\delta_{COL}$ and a_x/δ_{COL}.
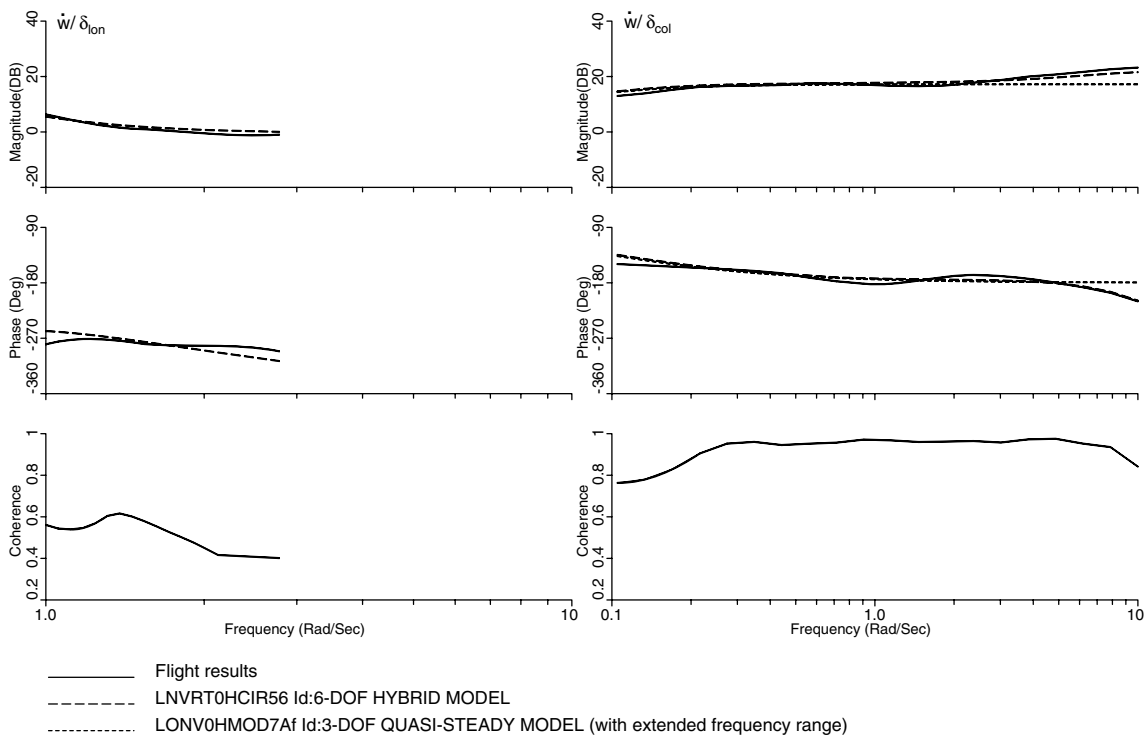
Figure 20. Comparison of quasi-steady and hybrid-model to flight data for $\dot{w}/\delta_{LON}$ and $\dot{w}/\delta_{COL}$.

Figure 19 shows that both models match the $\dot{u}/\delta_{COL}$ and a_x/δ_{COL} flight data for the range of frequencies used in each identification. Recall that for the quasi-steady model the frequency range was band-limited to 3 rad/sec so as to preclude the effects of dynamic inflow. However, for comparison purposes with the hybrid model the frequency range of the quasi-steady model was extended. The two models are compared up to a maximum frequency of 10 rad/sec. Between 2-10 rad/sec, it is observed that the hybrid model provides an improved fit in both magnitude and phase due to the inclusion of dynamic inflow.

As shown in Figure 20, the $\dot{w}/\delta_{COL}$ frequency response for both models fit the flight data well over their respective identification ranges. Because the quasi-steady model truncated the frequency to 3 rad/sec during the identification process, the phase roll-off observed at slightly higher frequencies is not present; as a result there was no need to model a time delay. Again, the hybrid model shows an improved fit in both magnitude and phase at higher frequencies as a result of including dynamic inflow.

4. Eigenvalues for the Hybrid Model

Table 15 presents the eigenvalues for the higher-order state-space model structure and Table 16 gives the roots for the second-order system used to model the rotor-on-rotor torque mode. Referring to Table 15, there are six real roots and three complex pairs for the hybrid state-space model.

The two poles at the origin (Eigenvalues 1 and 2) are integrators associated with coning kinematics. Eigenvalue 3 is the stable heave mode and its value is consistent with that of Z_w in Table 9. The complex poles (Eigenvalues 4 and 5) at a frequency of 0.614 rad/sec, are associated with a lightly unstable pitch phugoid mode. The left-half-plane pole at 1.43 rad/sec (Eigenvalue 6) is the stable (short-period) pitch-damping mode. The eigenvalues associated with inflow-coning dynamics result in identical values at the forward and rear rotors due to the simplifying assumptions described earlier, and will therefore be discussed collectively for both rotors.

Table 15. Eigenvalues of $\mathbf{M}^{-1}\mathbf{F}$ for the higher-order hybrid model at hover, HGW.

Eigenvalue	Real	Imaginary	Zeta (ζ)	Omega (ω_n) (rad/sec)	Mode
1	0.0000	0.0000	0.0000	0.0000	N/A
2	0.0000	0.0000	0.0000	0.0000	N/A
3	-0.1051	0.0000	0.0000	0.0000	Heave
4	0.1238	0.6009	-0.2017	0.6135	Phugoid
5	0.1238	-0.6009	-0.2017	0.6135	Phugoid
6	-1.4312	0.0000	0.0000	0.0000	Pitch-damping
7	-16.3475	0.0000	0.0000	0.0000	Fwd. Rotor Inflow
8	-16.3475	0.0000	0.0000	0.0000	Rear Rotor Inflow
9	-9.4913	14.8802	0.5378	17.6495	Fwd. Rotor Coning
10	-9.4913	-14.8802	0.5378	17.6495	Fwd. Rotor Coning
11	-9.4913	14.8802	0.5378	17.6495	Rear Rotor Coning
12	-9.4913	-14.8802	0.5378	17.6495	Rear Rotor Coning

The left-half-plane poles (Eigenvalues 7 and 8) at 16.347 rad/sec, are the forward and rear rotor inflow mode. The CIFER® identified inflow mode compares very well with the dynamic inflow research from Ref. 20. The stable complex pair (Eigenvalues (9, 10) and (11, 12)) are associated with the rotor flapping (coning) mode. In Ref. 20, Chen and Hindson show that when dynamic inflow is not included in the model structure, the frequency of the flapping mode occurs at approximately the 1/rev frequency; whereas this frequency is reduced when dynamic inflow is included. Furthermore, their research showed that variations in blade Lock number and thrust coefficient also cause the roots of this mode to migrate. For the values used in the hybrid model system identification ($\gamma = 8.8$ and $C_{T_0} = 0.007$), the eigenvalues for the flapping mode compare well with their research.

Table 16. Rotor-on-rotor torque dynamics.

	Real	Imaginary	Zeta (ζ)	Omega (ω_n) (rad/sec)
Numerator	-0.9142	7.5023	0.1210	7.5578
	-0.9142	-7.5023	0.1210	7.5578
Denominator	-1.7765	7.2352	0.2385	7.4501
	-1.7765	-7.2352	0.2385	7.4501

The rotor-on-rotor torque mode is described as a stable, yet lightly damped mode resulting from the forward rotor lagging while the rear rotor is leading. The result of modeling this mode as a lag-lead network yields a lightly damped complex-pair of zeroes, and complex-pair of poles— which agree with the description. The identification process results in a natural frequency of 7.45 rad/sec for this mode, which is within 10% error of the Boeing accepted value of 6.78 rad/sec. However, the identified mode frequency of 7.45 rad/sec does compare well with analytical results (~8.0 rad/sec) when a rigid drive system is assumed.

E. Time-Domain Verification

As discussed in Sec. II, the state-space hybrid model is verified against flight-test data which was not used in the identification process. Doublet maneuvers are preferred for verification purposes since the aircraft approximately returns to the initial trim state. In Figure 23 and Figure 24, the hybrid and quasi-steady models are compared to flight data for the longitudinal and collective doublets depicted in Figure 21 and Figure 22, respectively. For the longitudinal doublet maneuver, the hybrid model matches the aircraft vertical velocity very well, and tracks the vertical acceleration well—except for a slight over-prediction around 9 sec resulting from the collective input made at that moment. Both models match the longitudinal acceleration very well, but the quasi-steady model provides a closer match to the pitch rate, pitch attitude, and longitudinal velocity. Upon closer examination of these responses, the hybrid model produces a larger response to longitudinal inputs that the flight data. This can be seen in the frequency-domain as a slight over prediction in magnitude at low frequencies.

For the collective doublet, both models provide an excellent match to the aircraft response— this in spite of the band-limitation imposed on the quasi-steady model. However, examining the vertical acceleration response more closely, one can see that the hybrid model better matches the peak accelerations. For the vertical velocity response, the hybrid model is almost an exact match— which upholds the simplifying assumptions made in the dynamic inflow model for the vertical axis.
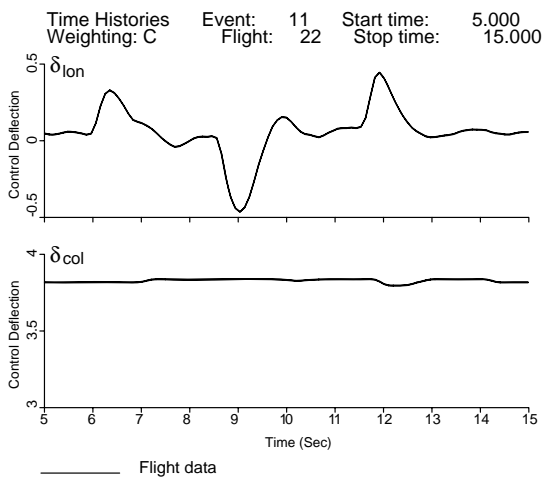

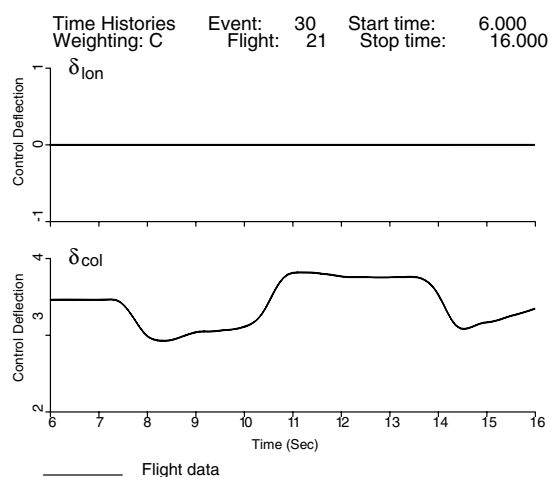Figure 21. Longitudinal doublet at mixer.
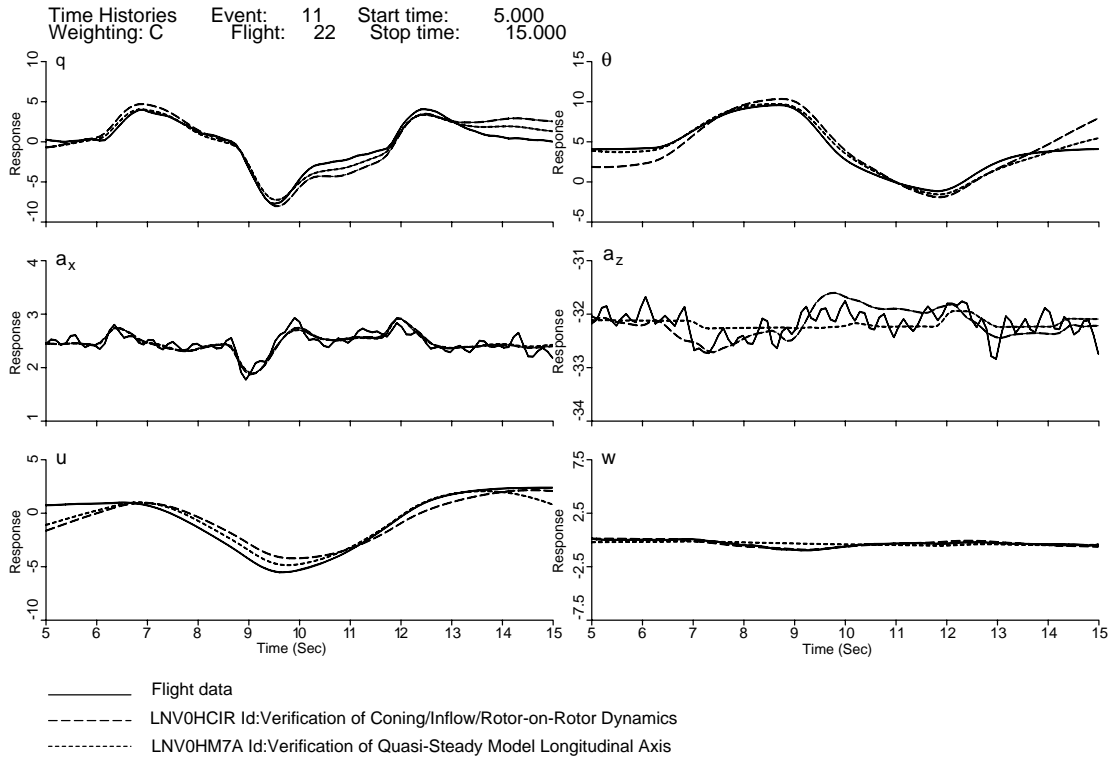

Figure 22. Collective doublet at mixer.

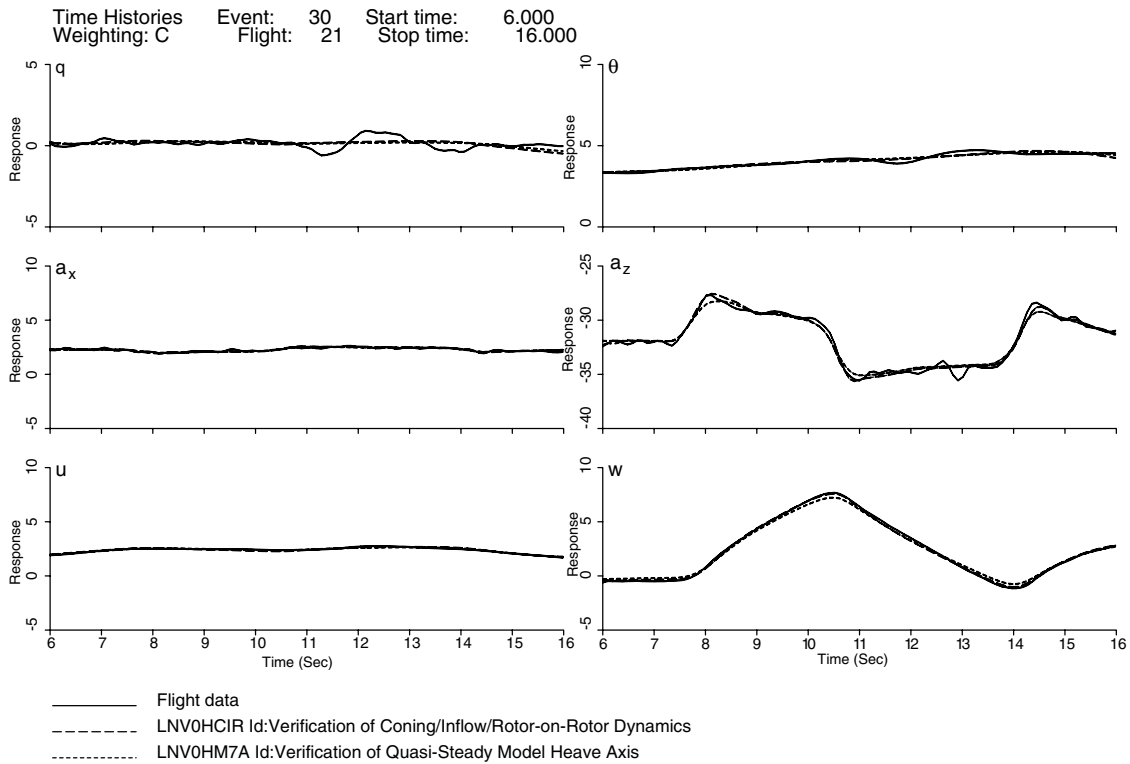**Figure 23. Comparison of quasi-steady and hybrid model for the longitudinal doublet.**

Figure 24. Comparison of quasi-steady and hybrid model for the collective doublet.

American Institute of Aeronautics and Astronautics

F. Discussion

This paper has developed two models of the CH-47F longitudinal response in hover. As can be seen by comparison with the on-axis flight response in Figure 18, the quasi-steady model provides an accurate representation up to a frequency of about 6 rad/sec. The more complex higher-order model extends the frequency range of applicability to 10 rad/sec. This section will consider the limitations of these models for flight control analysis and design.

A simple schematic diagram for the CH-47F flight control system is depicted in Figure 25. Pilot inputs are connected directly to the aircraft actuators via mechanical links. The combined aircraft and actuator system is represented by G(s) as obtained from the identification results. The stability and control augmentation system (SAS) provides improved stability, control response, and disturbance rejection. The SAS, represented by H(s), receives pilot commands and aircraft response measurements and generates additional input that is summed with the pilot's input via the ILCA SAS actuators.
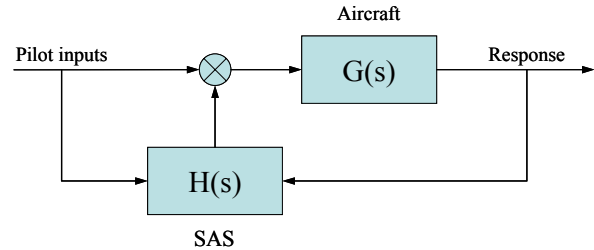

Figure 25. Simplified control schematic.

Figure 26 shows the root locus for the pitch rate feedback loop using the higher-order (hybrid) model. The bare-airframe pitch damping (M_q) is represented by the real pole at −1.43 rad/sec. Pitch rate feedback increases the damping to a value of −4 rad/sec for the nominal feedback gain of $K_q = 7$. The associated 0 dB crossover frequency is about 3.5 rad/sec with a phase margin of about 45 deg. At the same time the damping of the rotor coning dynamics is decreased to $\zeta = 0.3$. The values of rotor damping ratio and control system phase margin are at the limits of the MIL-F-9490D and ADS-33 limits, respectively, and suggest no further increases in gain are possible with the current PID feedback architecture. Instability is reached at a gain of $K_q = 32.4$, giving an ample gain margin of 13.3 dB.
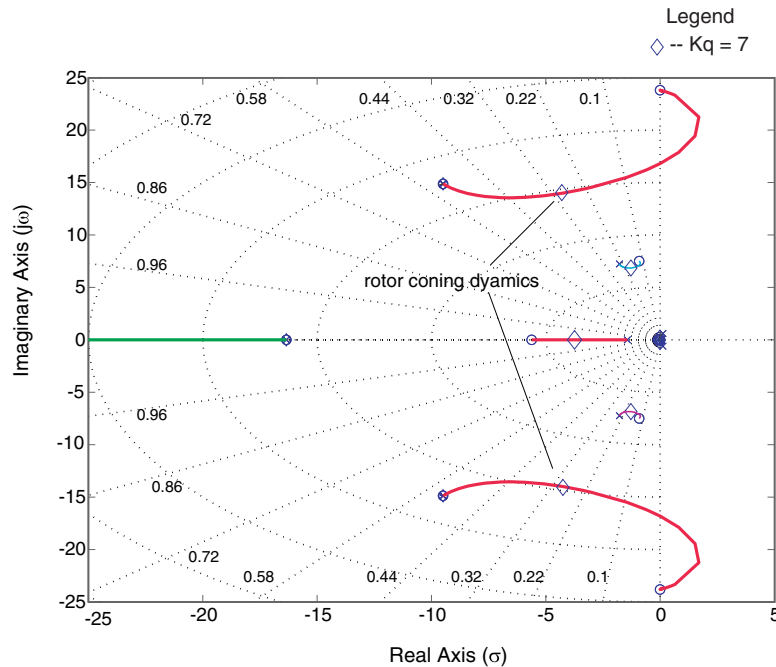

Figure 26. Root-locus for hybrid model.

The analogous pitch rate root locus for the quasi-steady model is shown in Figure 27. The pitch damping mode (M_q) is essentially the same as for the higher-order model. For the nominal gain, the predicted crossover frequency and phase margin is in agreement with the higher-order model. The gain margin is determined as 15.5 dB, which is somewhat over-predicted as compared to the more accurate higher-order model, but in either case the gain margin is quite sufficient.
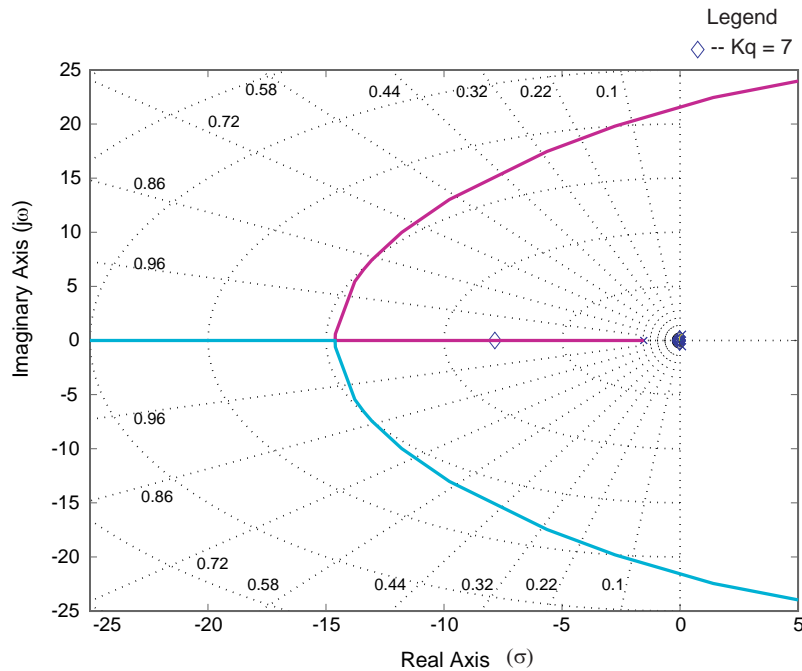
Figure 27. Root-locus for quasi-steady model.

The results herein indicate that the quasi-steady model is adequate for flight control analysis and design studies as documented in Ref. 8. However, the rotor dynamics are at the minimum of the requirement for damping ratio. Increased control system performance would be desirable for future CH-47 configurations; to achieve tighter command response and disturbance rejection would require a higher crossover frequency. This is achievable by trading off the excess gain margin for some increased phase margin, while carefully tailoring the influence on the rotor dynamics damping. Such studies would clearly require the use of the higher-order hybrid model.

VI. Conclusion

System identification studies were conducted based upon the frequency-domain flight-test data. State-space dynamics models of the CH-47F bare-airframe responses were determined for three weight conditions in hover and forward flight. Subsequently, the quasi-steady model was extended to include higher-order dynamics for the HGW configuration at hover. Both models provide a good representation of the CH-47F based on frequency-domain and time-domain comparisons. The following conclusions are drawn from this effort:

1) The CIFER® methodology to identifying a comprehensive state-space model at various airspeeds provides a simple and cost-effective approach to DAFCS development for the CH-47F.
2) A simple decoupled 3-DOF quasi-steady model proved to be sufficient for modeling the key flight mechanics of the CH-47F.
3) Additional degrees of freedom are necessary to better model the higher-order dynamics associated with dynamic inflow, rotor coning dynamics, and rotor-on-rotor dynamics.
4) A second-order lag-lead filter, optimized in the region of the mode, is sufficient to model the rotor-on-rotor torque dynamics. The availability of explicit engine torque/RPM dynamic data would have provided additional physical insight into the coupling of the rotor and drive systems, and would have permitted the modeling of the drive system dynamics directly into the state-space model structure.
5) The quasi-steady model is adequate for ongoing moderate gain control system designs. The higher-order model should be used for future high gain design studies.

Acknowledgments

References

[1] Keller, J. M., Hart, D. C., Shubert, M. W., and Feingold A., "Handling Qualities Specification Development for Cargo Helicopters," *American Helicopter Society 51st Annual Forum Proceedings*, Vol. 2, American Helicopter Society, Alexandria, VA, 1995, pp. 1747-1762.

[2] Anon., "Handling Qualities Requirements for Military Rotorcraft," Aeronautical Design Standard Performance Specification, ADS-33E-PRF, Aviation Engineering Directorate, US Army Aviation and Missile Command, Redstone Arsenal, AL, March 2000.

[3] Hoh, R. H., Mitchell, D. G., Aponso, B. L., Key, D. L., and Blanken, C. L., "Background Information and User's Guide for Handling Qualities Requirements for Military Rotorcraft," USAAVSCOM Technical Report 89-A-008, Aeroflightdynamics Directorate, US Army Aviation Research and Technology Activity, Ames Research Center, Moffett Field, CA, December 1989.

[4] Hoh, R. H., "ACAH Augmentation as a Means to Alleviate Spacial Disorientation for Low Speed and Hover in Helicopters," Presented at Heli-Japan – AHS International Meeting on Advanced Rotorcraft and Disaster Relief, 21-23 April, 1998, American Helicopter Society, Alexandria, VA, 1998.

[5] Howell, S. E., Howitt, J., and Gubbels, A. W., "Advances in Partial Authority Flight Control Augmentation," Defence Evaluation and Research Agency, United Kingdom, British Crown ©2001.

[6] Whalley, M., Howitt, J., and Clift, S., "Optimization of Partial Authority Automatic Flight Control Systems for Hover/Low-Speed Maneuvering in Degraded Visual Environments," *American Helicopter Society 55th Annual Forum*, Montréal, Canada, 25-27 May 1999, British Crown ©1999.

[7] Hoh, R.H., "Evaluation of Limited Authority Attitude Command Architectures for Rotorcraft," *American Helicopter Society 58th Annual Forum*, Phoenix, Arizona, 6-8 May 2003, American Helicopter Society, Alexandria, VA, 2003.

[8] Einthoven, P. G., Miller, D. G., Irwin, J. G., McCurdy, B. J., Bender, J., Blanken, C. L., Lawler, M. A., "Development of Control Laws for the Chinook Digital AFCS Program," American Helicopter Society 62nd Annual Forum, Phoenix, AZ, 9-11 May 2006, American Helicopter Society, Alexandria, VA, 2006.

[9] Tomashofski, C. A., and Tischler, M. B., "Flight Test Identification of SH-2G Dynamics in Support of Digital Flight Control System Development," *American Helicopter Society 55th Annual Forum*, Montréal, Canada, 25-27 May 1999, American Helicopter Society, Alexandria, VA, 1999.

[10] Tischler, M. B., and Remple, R. K., *Aircraft and Rotorcraft System Identification: Engineering Methods with Flight Test Examples*, AIAA 2006.

[11] Ham, J. A., Williams, J. N., and Tischler, M. B., "Flight Test Manual: Rotorcraft Frequency Domain Flight Testing," AQTD Project No. 93-14, US Army Aviation Technical Test Center, Sep. 1995.

[12] Bach, Ralph E. Jr., "State Estimation applications in Aircraft Flight-Data Analysis: A user's manual for SMACK," NASA RP-1252, Mar. 1991.

[13] Graham, D., and McRuer, D.T. *Analysis of Nonlinear Control Systems*, Dover Publications, 1971.

[14] Hamel, P.G. (ed.), *Rotorcraft System Identification*, AGARD-AR-280, 1991.

[15] Klein, V. and Schiess, J.R, "Compatibility Check of Measured Aircraft Responses Using Kinematic Equations and Kalman Filter", NASA TN D-8514, 1977.

[16] Tischler, M. B. and Cauffman, M. G., "Frequency-Response Method for Rotorcraft System Identification: Flight Applications to the Bo-105 Coupled Rotor/Fuselage Dynamics," Journal of the American Helicopter Society, Vol. 37, No. 3, July 11, 1992, pp. 3-17.

[17] Tischler, Mark B., "Frequency-Response Identification of XV-15 Tilt-Rotor Aircraft Dynamics," NASA TM 89428, May 1987.

[18] Tischler, M. B., "System Identification Requirements for High-Bandwidth Rotorcraft Flight Control System Design," Journal of Guidance, Control, and Dynamics, Vol. 13, No. 5, Sep.-Oct. 1990, pp. 835-841.

[19] Gaonkar, G. H., and Peters, D. A., "Review of Dynamic Inflow and Its Affect on Experimental Correlations," Proceedings of the 2nd Decennial Specialists' Meeting on Rotorcraft Dynamics, NASA-CP-2400, NASA Ames Research Center, 1984, pp. 187-205.

[20] Chen, R. T. N., and Hindson, W. S., "Influence of Dynamic Inflow on the Helicopter Vertical Response," Vertica, Vol. 11, No. 1/2, pp. 77-91, Pergamon Journals Ltd., Great Britain, 1987.

[21] Chen, R. T. N., "Effect of Primary Rotor Parameters on Flapping Dynamics," NASA-TP-1431, NASA Ames Research Center, Jan. 1980.

[22] Miller, D. G., and White, F., "A Treatment of the Impact of Rotor-Fuselage Coupling on Helicopter Handling Qualities," American Helicopter Society 43rd Annual Forum, St. Louis, MO, 18-20 May 1987, American Helicopter Society, Alexandria, VA, 1987.